

# Blazars SED in Conical Plasma Flow : a Monte Carlo study

Nagendra Kumar<sup>1\*</sup>

Pankaj Kushwaha<sup>2 †</sup>

<sup>1</sup>Department of Physics, Indian Institute of Science, Bangalore 560012, India

<sup>2</sup>Aryabhata Research Institute of Observational Science (ARIES), Nainital 263002, India

## Abstract

Blazars host the most powerful persistent relativistic conical jet– a highly collimated anisotropic flow of material/plasma. Motivated by this, we explore the blazar’s broadband spectral energy distribution (SED) in an anisotropic flow of plasma which emits via synchrotron and inverse Compton (IC) mechanism. The flow is conical with two velocity components: a highly relativistic flow component along the jet axis and a random perpendicular component with average random Lorentz factor  $\langle \gamma^{ran} \rangle \ll$  than the average component along the jet axis  $\langle \gamma \rangle$ . Assuming a broken power-law electron population, we calculated the broadband SED using synchrotron and IC processes assuming a cylindrical (of radius R and length L) emission region. For the IC process, we used Monte Carlo approach. We found that such anisotropic flow can reproduce blazars broadband emission as well as general short and high amplitude variability, indicating that spectral and temporal variability are not sufficient to distinguish among existing models. We demonstrate this by reproducing SEDs of FSRQ 3C 454.3 and three BL Lacs objects OJ 287, S5 0716+714, PKS 2155-304. Our formalism and set-up also allow us to investigate the effect of the geometry and dimension of emission region on observed broadband spectra. We found that the SEDs of low synchrotron peak (LSP) blazar can be explained by considering only SSC (synchrotron self-Compton) if R/L ( $< 0.01$ ), broadly mimicking a spine-sheath geometry. In general, the degeneracy between non-thermal particle number density and length of the emission region (L) allow us to reproduce any variability in terms of particle number density.

**Key words:** radiation mechanisms: non-thermal - gamma rays: galaxies - galaxies: jets - galaxies: active - quasars: individual:3C 454.3 - BL Lacertae objects: individual: OJ 287, S5 0716+714, PKS 2155-304

## 1 Introduction

Blazar, comprising of BL Lacertae objects (BLLs) and flat spectrum radio quasars (FSRQs), is a subclass of active galactic nuclei with a highly collimated relativistic jet of plasma aligned at close angles to our line of sight. They are characterized by a high and rapidly variable continuum, exhibiting a broad double-humped spectral energy distribution (SED,  $\nu$  vs  $\nu F_\nu$ ) extending from radio to GeV/TeV  $\gamma$ -ray energies. The low-energy hump extends from radio to ultraviolet (UV)/X-ray with a maximum in between near-infrared (NIR) to UV/X-rays while the high-energy hump spans X-rays to GeV/TeV  $\gamma$ -rays with a maximum at sub-GeV to GeV energies. The radio and optical emission, which constitute the low-energy hump show high and variable polarization, and thus, is widely regarded as synchrotron emission from the relativistic non-thermal electrons in the jet. The characteristic double-humped SED and an apparent positive correlation between the maximum of the two humps have led to an additional classification scheme based solely on this (Fossati et al. 1998). Thus, based on the location ( $\nu_s$ ) of the maximum of the low-energy hump, blazars have been termed low-synchrotron peaked (LSP,  $\nu_s \leq 10^{14}$  Hz), intermediate-synchrotron peaked (ISP,  $10^{14} < \nu_s < 10^{15}$  Hz), and high-synchrotron peaked (HSP,  $\nu_s > 10^{16}$  Hz). However, so far only BLLs have been found to conclusively show the three spectral subclassed, referred respectively as LBL, IBL, and HBL while FSRQs are exclusively LSP.

\*nagendra.bhu@gmail.com

†pankaj.kushwaha@aries.res.in

For the high-energy hump, two competing scenarios, broadly referred to as leptonic and hadronic, depending on the primary particles responsible for the high energy emission have been proposed in the literature. In the leptonic scenario, entire blazar emission is due to electrons (or positrons) and it is one of the widely considered scenario due to presence of the synchrotron emitting relativistic electrons and a wide range of soft photon fields from different AGN constituents. It attributes the X-rays and  $\gamma$ -rays to the up-scattering of the local soft-photon fields by electrons through inverse Compton (IC) mechanism (e.g. [Ghisellini & Tavecchio 2009](#); [Kushwaha et al. 2013, 2018a](#)). The widely considered soft-photon fields include synchrotron photons in the jet and photons external to the jet e.g. from AGN constituents like accretion disk (AD), broad line region (BLR), IR torus (IR), and the omnipresent cosmic microwave background (CMB) photons. Accordingly, their respective IC spectra are generally referred in literature as synchrotron self-Compton (SSC), EC-AD, EC-BLR, EC-IR, and EC-CMBR where EC stands for external Comptonization – IC of photon fields external to the jet. Depending on the location of emission region, one or many of the soft photon fields may contribute significantly to the observed emission. The alternative scenario based on hadronic interactions attributes the high energy hump to proton-synchrotron and/or cascades initiated as a result of hadron-hadron and hadron-photon interactions (e.g. [Böttcher et al. 2013](#), and references therein).

Based on these two scenarios, a variety of models, time-dependent and time-independent have been proposed in the literature for the double-humped SEDs. The time-dependent model additionally provides insights into the likely jet physical conditions and processes causing the observed changes by attempting to reproduce additional observational quantities like light curves (e.g. [Kushwaha et al. 2014](#)), polarization evolution (e.g. [Chandra et al. 2015](#)) etc. or the general observational trends (e.g. [Marscher 2014](#)). The time independent model, on the other hand, only concerned with reproducing the observed SED, and can be broadly considered as a snapshot moment of the time dependent models.

A huge range of rarely repeating observational behaviors exhibited by these sources combined with enormous scale of separation between the extremes suggest a very diverse and extreme jet physical conditions. On one hand, magnetic field is believed to play an important and dominant role in the formation and collimation of relativistic jets close to the central engine, broadband SEDs modeling suggests a kinetically dominated jet. Despite the importance of magnetic field in jets, its configuration is still uncertain, however the polarization measurement for low energy hump emission (or synchrotron radiation) suggest, in many cases, a helical magnetic field configuration (e.g., [Lyutikov et al. 2005](#); [Gabuzda 2017](#)). Further, though we have a general understanding and idea of relevant physical conditions and radiation processes in the jet, we still lack a comprehensive understanding. All the models proposed in the literature for emission or observed behaviors are primarily specific, with limited applicability—capable of explaining a few of the observed features/trends or explain the general features e.g. stochastic variability (e.g. [Marscher 2014](#)) etc. Specifically, apart from the beamed emission it is expected that the emission model must explain the observed features like variability time scale and at the same time, should be optically thin to pair production (see, [Maraschi et al. 1992](#); [Dondi & Ghisellini 1995](#), and references therein) given the fact that the shortest variability time scale provides a maximum bound on the size of the emission region, which is usually order of hours to days.

From the observer point of view, as the jet appears in radio images, its a conical collimated flow i.e. an anisotropic flow. The strong kinetic dominance inferred in a few cases ([Algaba et al. 2019](#)) suggests an anisotropic flow locally. Whether such a local anisotropic flow can emit powerfully can be determined by its capability to produce the emission with observed features within the known observational constraints. Also how it accelerates anisotropically, is still an open issue. In literature, attempts have been made to understand an anisotropic particle acceleration (e.g., [Armstrong et al. 2012](#); [Yang & Zhang 2018](#)). In this work, we focus solely on the emission aspect with assuring that within the emission region the flow is stable in assumed magnetic field configuration— wiggler plus axial magnetic field. In helical undulator (or free-electron laser) principle, the anisotropically moving relativistic electron emits THz radiation (even X-ray emission, e.g., [Pellegrini et al. \(2016\)](#)) in the presence of wiggler plus axial magnetic field (verified in laboratory). Motivated from the helical undulator principle we assume that the conically moving electron will emit synchrotron radiation in presence of a wiggler (acting in plane perpendicular to the jet axis) plus axial magnetic field. Though the formulation of helical undulator is non-linear it assures (proven experimentally) that when one of electron velocity component is along the wiggler field direction and another one is along the axial field direction then electron moves on stable orbit along the wiggler field path without changing the magnitude of both the velocity components (e.g., [Ginzburg & Peskov 2013](#); [Balal et al. 2015](#), and references therein). However, a polarization measurement for synchrotron

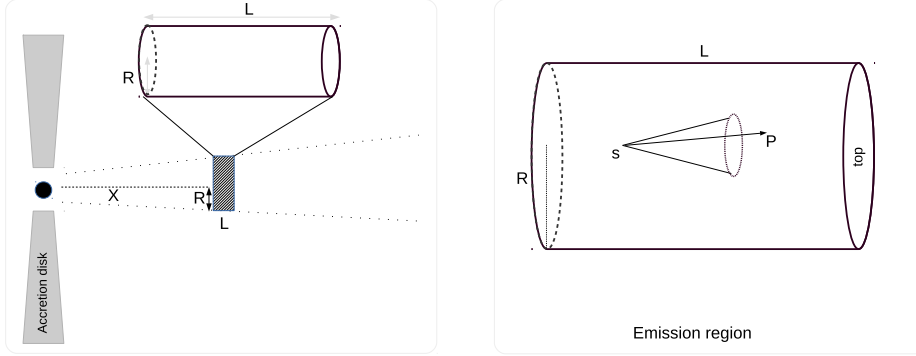


Figure 1: *Left*: A cartoon diagram of a conical jet with a semi aperture angle of  $\theta_j$  and the embedded emission region marked by a shaded area of length  $L$ . The emission region is at  $X$  distance from the central engine. Since  $L \ll X$ , the shape of emission region can be approximated to a cylindrical (its zoomed version has been shown, where  $R$  is the radius and  $L$  is the length of the cylinder). *Right*: The motion of jet-matter inside the cylindrical emission region. At any point  $s$  inside the emission region, the flow lies inside the cone of angle  $\theta_j$ . One such directions on the surface of cone is shown by the arrow  $sP$  (see Kumar 2018). The face marked *top* is the face of emission region towards the observer.

radiation in wiggler + axial magnetic field is needed to establish the viability of this field configuration in the jet environment. We intended to study this in future. In this work, we explore this scenario by considering a local conical flow and model the SED assuming leptonic emission processes. We show that the synchrotron emission is beamed (but not due to a bulk Doppler boosting) and IC process dominates over the pair production process. In the next section, we present the details of model and geometry of the emission region. §3 presents the SED modeling approach and §4 discusses the comparison of observed SED of blazars followed by our summary and conclusions in §5.

## 2 Emission mechanism of the conical jet model

Motivated by the observed jet morphology in radio observations, we assumed a conical jet of opening angle or semi-aperture angle  $\theta_j$ , as shown in figure 1, where the emission region (responsible for the observed emission) is embedded in the flow. The emission region is located  $X$  distance from the central engine (shaded region in figure 1) and usually lie beyond the acceleration region. Within it electrons have attained the relativistic conical flow now steadily. Our primary goal is to generate the SEDs of blazar in leptonic model having a steady conically flowing relativistic electron inside the emission region. The maximum size of emission region  $L$  is usually estimated from the flaring phase of blazars and is order of  $\gamma$ -ray variability time scale ( $\sim$  hours to days). As per current understanding from spectral and temporal studies, blazar's emission region is widely agreed to be mainly at sub-parsec or parsec scales i.e.  $X \gtrsim 0.1$  pc (e.g. Marscher 2006; Ghisellini & Tavecchio 2009; Agudo et al. 2013; Ghisellini et al. 2014). Thus, for a compact emission region ( $L \ll X$ ), one can approximate the conical emission region ( $R_{\text{top}} > R$ ) to a cylindrical ( $R_{\text{top}} = R$ , here  $R$  and  $R_{\text{top}}$  are the radius of emission region of the base and top face respectively, and  $\frac{R_{\text{top}}}{R} = 1 + \frac{L}{X}$ ). Without any loss of generality, in our calculation we have considered a cylindrical emission region of radius  $R$  and length  $L$  (as shown in figure 1).

Since the flow is conical, it has two velocity components: one along the jet axis which is the dominant one and the other perpendicular to it. The corresponding Lorentz factors are  $\gamma$  and  $\gamma^{ran}$  respectively (i.e., the particle is moving mainly along the jet axis with Lorentz factor  $\gamma^R$  which corresponds to its composite velocity  $v_R$  of both components  $v$  and  $v_{ran}$ , as  $v_R = \sqrt{v^2 + v_{ran}^2 - v^2 v_{ran}^2 / c^2}$  or  $\gamma^R = \gamma \gamma^{ran}$ ). The direction of dominant velocity component is defined same to that in Kumar (2018) (see also, Kumar 2017), and one of its directions is shown by  $sP$  vector in the right panel of figure 1. The other component lies in the plane perpendicular to the vector  $sP$  and points randomly in this plane (not shown here for clarity). Our main focus here is to explore the spectral and temporal behavior in an anisotropic flow (e.g., Yang & Zhang 2018), dominated by the velocity component along the jet axis and all quantities

refer to the measurement in the observer's frame.

## 2.1 Synchrotron emission

The anisotropically moving relativistic electrons will emit the synchrotron emission in presence of magnetic field and also up-scatter the local soft photon fields via IC. In many observations, the jet polarization indicates that the flow carries helical magnetic fields (e.g., Lyutikov et al. 2005; Gabuzda 2017). As discussed in the introduction, the helical periodic magnetic field (wiggler,  $B_w(\mathbf{i} \cos(k_w z) + \mathbf{j} \sin(k_w z))$ , here  $B_w$  is the amplitude of wiggler field and  $2\pi/k_w$  is the wiggler period) along with axial magnetic field ( $\mathbf{k} B_o$ , here  $\mathbf{i}, \mathbf{j}, \mathbf{k}$  are the cartesian axis where  $\mathbf{k}$ -direction along the jet-axis) is a promising field configuration to generate the synchrotron emission by anisotropically moving electrons, and has been extensively studied in the case of a helical undulator (e.g., Balal et al. 2015; Ginzburg & Peskov 2013).

Similar to the synchrotron emission mechanism in helical undulator, we consider that the random velocity component ( $v_{ran}$ ) of electrons is along the wiggler field direction. In that situation electron will move on stable helical trajectory (which is along the wiggler field) with constant axial speed (i.e., dominant velocity component) and having constant of motion,  $\gamma^R m_e c = \text{constant}$ . In the appendix we have revisited the single electron trajectory in a wiggler + axial field. The synchrotron radiation is emitted in forward direction with frequency  $(\gamma^R)^2 \nu_b$  (where  $\nu_b = \frac{e B_o}{2\pi m_e c}$  is a Larmor frequency,  $e$  is the electronic charge,  $m_e$  is the mass of electron,  $c$  is the speed of light). The resulting synchrotron radiation will be beamed in the forward direction along the jet axis. The efficiency of emission depends on the ratio of cyclotron frequency ( $\nu_b \gamma^R$ ) to the bounce frequency ( $\Omega_b = v k_w$ ) (e.g., Balal et al. 2015; Ginzburg & Peskov 2013). Here, we would stress that for SSC spectrum calculation we consider observed synchrotron emission as a seed photons and  $\gamma^R$  is determined from the observed SED shape. In another way, here, we surmise that wiggler + axial magnetic field configuration in jet environment is efficient to generate the synchrotron emission by anisotropically moving relativistic electron.

As per the observed blazars SED shape (low-energy hump), we assumed a broken powerlaw distribution for a synchrotron emitting electrons, defined by

$$N'(\gamma^R) d\gamma' = \begin{cases} K (\gamma^R)^{-p} d\gamma' & ; \gamma'_{min} < \gamma^R \leq \gamma'_b \\ K \gamma'_b{}^{q-p} (\gamma^R)^{-q} d\gamma' & ; \gamma'_b \leq \gamma^R < \gamma'_{max} \end{cases}$$

where, the electron Lorentz factor  $\gamma^R$  is in the range of  $\gamma'_{min}$  to  $\gamma'_{max}$  and  $\gamma'_b$  corresponds to the break in the distribution.  $p$  and  $q$  are the powerlaw indices of the electrons, before and after the break respectively.  $K$  is the normalization factor which is related to the total electron density inside the  $\gamma$ -ray emitting region as

$$n_e = \frac{K}{p-1} (\gamma'_{min}{}^{1-p} - \gamma'_b{}^{1-p}) \quad (1)$$

With  $q > p$  and  $p > 1$ , as is the case with blazars SEDs, if  $\gamma'_b \gg \gamma'_{min}$  then  $n_e \left( \approx \frac{K}{p-1} \gamma'_{min}{}^{1-p} \right)$  will depend on  $\gamma'_{min}$  and  $p$ . In our model (i.e., in the observer's frame) the peak frequency of synchrotron spectrum  $\nu_p^{syn}$  is given as

$$\nu_p^{syn} = \frac{\gamma'_b{}^2}{1+z} \nu_B \quad (2)$$

with  $z$  being the redshift of the source. Similarly the synchrotron frequency corresponding to  $\gamma'_{min}$  and  $\gamma'_{max}$  is defined as  $\nu_{min}^{syn} = \frac{\gamma'_{min}{}^2}{1+z} \nu_B$ ,  $\nu_{max}^{syn} = \frac{\gamma'_{max}{}^2}{1+z} \nu_B$  respectively.

Further, we assumed that the magnitude of the random velocity component of electron is constant for simplicity. Since  $\gamma^R = \gamma \gamma^{ran}$ , the forward velocity component of electron will follow also the broken powerlaw distribution as given below

$$N(\gamma) d\gamma = \begin{cases} K \gamma^{-p} d\gamma & ; \gamma_{min} < \gamma \leq \gamma_b \\ K \gamma_b{}^{q-p} \gamma^{-q} d\gamma & ; \gamma_b \leq \gamma < \gamma_{max} \end{cases} \quad (3)$$

where, the Lorentz factor of electron's forward conical velocity component  $\gamma$  is in the range of  $\gamma_{min}$  to  $\gamma_{max}$ .  $\gamma_b$  corresponds to the break in the distribution and these are related to the electron Lorentz factor as  $\gamma'_{min} = \gamma_{min} \gamma^{ran}$ ;  $\gamma'_b = \gamma_b \gamma^{ran}$ ;  $\gamma'_{max} = \gamma_{max} \gamma^{ran}$ . Similarly, the synchrotron frequency

is expressed as  $\nu_p^{syn} = \frac{\gamma_b^2(\gamma^{ran})^2}{1+z}\nu_B$ ;  $\nu_{min}^{syn} = \frac{\gamma_{min}^2(\gamma^{ran})^2}{1+z}\nu_B$ . The average Lorentz factor for dominant velocity component of electron  $\langle\gamma\rangle$  is given by  $\langle\gamma\rangle = \frac{\int\gamma N(\gamma)d\gamma}{\int N(\gamma)d\gamma}$ . Since, we are interested in exploring blazar's SED from an anisotropic motion of electrons, to ensure the anisotropic motion of electron we fix  $\gamma^{ran}$  to  $\gamma_{min}/2$ . Further, since the electron Lorentz factor  $\gamma^R$ , also  $\gamma$ , follows the broken powerlaw distribution, for generality (without affecting the results, see figure 3b of subsection 3.2.1) we assume that the random velocity component follows a uniform distribution in range  $[\gamma_{min}^{ran}, \gamma_{max}^{ran}]$  with  $\gamma_{max}^{ran} = \gamma_{min}$  and  $\gamma_{min}^{ran} \ll \gamma_{min}$ , thus the mean  $\langle\gamma^{ran}\rangle$  ( $= \frac{\gamma_{min}^{ran} + \gamma_{max}^{ran}}{2}$ )  $\approx \gamma_{min}/2$ .

For a well observed SED from mm to  $\gamma$ -ray energies, the low-energy hump being synchrotron emission provides a direct relation to infer the particle spectral indices if NIR-optical part is not heavily contaminated by the thermal components (e.g. BLR and IR torus for LSP sources). However, currently we have better coverage and observational cadence in NIR-optical and often in X-rays. Since the NIR to X-ray emission, for all the three blazars spectral classes, covers emission before and after spectral break in the leptonic emission scenario, the particle spectral indices can be inferred fairly well from spectrum in these parts (e.g. Kushwaha et al. 2013).

## 2.2 IC process and Monte Carlo Method for IC spectrum

The presence of a diverse range of soft photon fields from different AGN constituents and the relativistic synchrotron emitting electrons provide a natural environment for high energy emission via IC scattering. We assumed this scenario for the broadband emission, i.e. entire emission due to synchrotron and IC. Since, the conically moving relativistic electrons emit the synchrotron radiation in forward direction (in presence of wiggler + axial magnetic field), we consider a conical direction with same semi aperture angle  $\theta_j$  (in similar way as described in figure 1) for a synchrotron photon direction. That is, for a given scattering site, the direction of synchrotron photon is any one of directions on the surface of cone at that site. The optical depth ( $\tau$ ) for IC (in cylindrical emission region) is defined along the jet-axis, i.e.,  $\tau = L n_e \sigma_T = L/\lambda$ , here  $\sigma_T$  is the Thomson cross section,  $\lambda$  is the mean free path of photons. We have computed the mean free path of photons considering only forward conical velocity component of electron for SSC.

For EC, we assumed an isotropic external photon field approximated by a blackbody. Using a more elaborate geometry of external photon field doesn't change the outcome significantly (e.g. Böttcher et al. 2013). The mean free path of photons has been computed considering the composite velocity of electron for EC. We are computing the time-averaged IC spectrum over the time  $L/c$ , we have populated the scattering event homogeneously inside the emission region. However, we compute the time-averaged IC spectrum for both flaring and quiescent phase spectrum. Physically, after the time  $L/c$ , electrons would be cooled by both synchrotron and IC process and one can expect the evolution of the spectra from flaring phase to quiescent. In present study, to avoid the complexity, the evolution of spectra has not been studied, which we are intended to study in future.

In the present scenario, in IC process the photons get up-scattered by both the velocity components (first formulated by Blandford & Payne 1981; for high energies X-ray emission mechanism in X-ray binaries, Titarchuk et al. 1997; Kumar 2017) of electron. To estimate the IC spectrum from different photon fields, we followed the Monte Carlo, MC, approach developed by Kumar (2018, 2017, and references therein), with appropriate modifications for the relativistic scattering regime. Further, in case of IC calculation (only for computational simplicity), we have allowed the random component to be in any plane rather than restricting in plane perpendicular to the forward velocity vector. Since, if one computes the IC spectrum considering the random velocity component either strictly in the perpendicular plane of the axial velocity or any plane, then in both cases the IC spectrum will be similar. In this work, we have computed the spectrum for fixed opening angle of conical flow, i.e., jet opening angle.

For the assumed geometry, flow and seed photon fields, the rear-end scattering will dominate for SSC process while the isotropic scattering in EC process. In rear-end IC scattering, photon gains lesser energy compared to the head-on scattering. Thus, it is expected that for modeling the same SED of blazar the required Lorentz factor for SSC would be much larger in comparison to the respective EC dominated values (see, §4.1, §4.3).

Electron direction can change after a scattering in IC process, which may alter the synchrotron emission or conical flow's direction. In IC process, for highly relativistic electron ( $\gamma \gg 1$ ) and low-energy unscattered photon ( $E_p \ll m_e c^2$ ,  $E_p$  is the photon energy), which is our considered case, the

scattered photon is always in the unscattered electron's direction. In addition, the scattered electron and photon are in same direction (Pozdnyakov et al. 1983, see also Kumar & Misra 2016). Hence, the electron direction does not get alter after IC process in our framework, i.e., it will maintain the conical flow, and the synchrotron emission is always beamed in forward direction.

The spectral peak frequency of SSC in the assumed scenario for single scattering is given by  $\nu_p^{ssc} \propto \langle \gamma^2 \rangle \langle \gamma^{ran} \rangle^2 \langle \nu_p^{syn} \rangle$ , where  $\langle \nu_p^{syn} \rangle = \langle \gamma^2 \rangle \langle \gamma^{ran} \rangle^2 \nu_B$  is an average seed synchrotron photon frequency for SSC; and  $\langle \gamma^2 \rangle = \frac{\int \gamma^2 N(\gamma) d\gamma}{\int N(\gamma) d\gamma}$ . Here, we consider a proportionality relation for  $\nu_p^{ssc}$  (usually,  $\nu_p^{ssc} \approx (1 - \frac{v}{c})^2 \langle \gamma^2 \rangle \langle \gamma^{ran} \rangle^2 \langle \nu_p^{syn} \rangle$  for rear-end scattering), mainly because of that  $\nu_p^{ssc}$  also depends on  $\theta_j$  of conically moving relativistic electron (as, Kumar 2018 has shown that IC spectra for rear-end scattering becomes harder by increasing  $\theta_j$  for a given electron energies). We have checked the proportionality relation for  $\nu_p^{SSC}$  in two ways in Monte Carlo method. In first case we change  $\langle \gamma^{ran} \rangle$  in such a way that  $\langle \gamma^2 \rangle$  is unchanged (see figure 3c of subsection 3.2.1) and in second we change  $\gamma_{min}$  (see figure 4c of subsection 3.2.2). In case of EC process, the IC scattering is an isotropic so the scattered frequency would be independent of  $\theta_j$ . The peak frequency of EC  $\nu_p^{EC}$  for single scattering is simply determined by the relation  $\nu_p^{EC} \approx \langle \gamma^2 \rangle \langle \gamma^{ran} \rangle^2 \nu_p^{bb}$ , here  $\nu_p^{bb}$  is the peak frequency of the blackbody emission at temperature  $T_{EC}$  (see subsection 4.1 and table 1 for MC results).

### 2.3 Optically thin IC spectrum calculation

In the IC scattering, the mean free path of photons inside the electron scattering medium increase with electrons speed. Especially, for  $\gamma > 10$ ,  $\lambda$  increases rapidly, e.g.,  $\lambda$  is  $\sim 6.0 \times 10^{17}$ ,  $5.8 \times 10^{19}$ ,  $5.7 \times 10^{21}$  cm for  $\gamma = 10, 100, 1000$  respectively for  $10^{15}$  Hz photon at  $n_e = 10^8 \text{ cm}^{-3}$  (e.g., Kumar 2018). In general, the mean free path of the particle in medium is inversely proportional to the medium density and total differential cross-section. Further, for a given electron population there exists a minimum average scattering number ( $\langle N_{sc} \rangle$ ) after which the photons energy spectrum does not change with increasing  $\langle N_{sc} \rangle$ . This resulting limiting photons spectra are referred as Wien's peak spectra. Similar to the case of variation of mean free path, the Wien peak spectrum in ultra relativistic limit occurred for a low value of minimum  $\langle N_{sc} \rangle$  (e.g., the minimum  $\langle N_{sc} \rangle \sim 10, \sim 6$  and  $\sim 2$  for  $\gamma = 20, 100$  and  $1000$  respectively), while in non-relativistic limits Wien peak is observed for a large value of  $\langle N_{sc} \rangle$  (e.g., Kumar & Misra 2016). In this work we will compute/compare the SED almost single scattering limit, i.e., very far from the Wien's peak spectrum limit, or in optically thin regime. The MC treatment already takes all the special relativistic effect. We only need to apply the redshift to the emitted spectrum to transform it to the observed one.

### 2.4 The pair production

Pair production is an another competing process which may affect observed SEDs as the  $\gamma$ -ray produced by Compton process will get disappeared by producing  $e^+e^-$  pairs if the threshold energy value for the two photons ( $E_{p1}, E_{p2}$ ) becomes  $\geq 2m_e c^2$  i.e.  $E_{p1} + E_{p2} \geq 2m_e c^2$  where  $m_e$  is the mass of an electron/positron, and  $E_{p1} = h\nu_{p1}$  with  $h$  being the Planck constant. The cross section for pair production is given by (e.g., Aharonian et al. 2008; Pozdnyakov et al. 1983)

$$\sigma_{\gamma\gamma} = \frac{3\sigma_T}{8s} \left[ \left( 2 + \frac{2}{s} - \frac{1}{s^2} \right) \ln(\sqrt{s} + \sqrt{s-1}) - \left( 1 + \frac{1}{s} \right) \sqrt{1 - \frac{1}{s}} \right]$$

Here  $s = \frac{E_{p1}E_{p2}}{m_e^2 c^4} \approx \frac{\nu_{p1}\nu_{p2}}{1.52 \times 10^{40} \text{ Hz}^2}$  and the above mentioned threshold corresponds to  $s = 1$ . Thus,  $\sigma_{\gamma\gamma} = 0$  for all  $s \leq 1$  (threshold) and at  $s = 2$  the cross section for pair production has maximum  $\sigma_{\gamma\gamma} = 0.25\sigma_T$ . From threshold  $s = 1$ , we can see that photons of frequency less than  $10^{12}$  Hz needs a photon of energy  $> 10^{28}$  Hz ( $\sim 41$  TeV) to produce  $e^+e^-$  pair, but observed spectra of a majority of blazars normally extend up to a few hundreds of GeVs. The other crucial factor is the number density of the soft photons which, in general, follow a monotonic declining trend with some powerlaw form or steeper from NIR to GeV/TeV energies. For example, when the electron energy distribution has single powerlaw distribution with index  $p$ , the synchrotron photon density is proportional to  $\nu^{-(p-1)/2}$  (e.g., Shah et al. 2017), so for  $p=2$  the synchrotron photon density at  $10^{14}$  Hz (or,  $\geq 10^{14}$  Hz) is almost 10 times smaller than that at  $10^{12}$  Hz (or,  $\geq 10^{12}$  Hz). As a result, photons of frequency  $10^{26}$  Hz will see 10 times

smaller photon density for pair production in comparison to the  $10^{28}$  Hz photons. Other way around, the probability for pair production by  $10^{26}$  Hz photons via photon-photon scattering is almost 10 times lesser when it is done by  $10^{28}$ Hz. Further, the cross section for pair production ( $\sigma_{\gamma\gamma}$ ) is smaller than IC cross section. Thus, in the optically thin regime i.e. in the single scattering limit, the pair production will be negligible.

### 3 General Results and SED Calculation

In the leptonic emission scenario, the location of emission region plays a crucial role in deciding the role of external photon fields as seed photons for IC. In general, it is inferred from the modeling of the SEDs (e.g. Ghisellini & Tavecchio 2009; Kushwaha et al. 2013). Rather than deriving the temperature from SED fitting, we tested two temperature – 500 K and 50k K, representative of IR torus and BLR field.

As it turned out, for the assumed cylindrical geometry of the emission region, its length (L) vis-a-vis mean free path ( $\lambda$ ) has strong effect on the direction of emitted synchrotron photons and hence, SSC as well. The next subsection (§3.1) explore this aspect. Other uncertainties in the model are effects of use of limited energy range of synchrotron emission for calculating SSC spectrum, arbitrariness of the subdominant random velocity components on the model generated IC spectrum, and the effect of dimension of emission region. We investigate these in the subsection §3.2. It should be noted that in both these subsections, we do not focus on constraints from blazar observations but only on the effects of these uncertainty on the model generated spectrum. After these assessment, we consider modeling blazar SEDs using observational constraints in §3.3.

#### 3.1 Estimation of observed synchrotron emission

The observed synchrotron emission is total synchrotron photons generated inside the cylindrical emission region minus those that got IC scattered to higher energies. Further, since synchrotron emission is mainly in forward direction along the jet axis, most of the emitted photons will exit from the face of the cylinder closer to the observer. Both of these depend on the geometry and dimension of the emission region (scattering region) as shown in figure 2 as well as the optical depth for SSC, which is measured along the length L. For a given  $\lambda$ , the unscattered photons existing from the front face will first increase and after reaching the maximum it will decrease with increasing L (as shown by curve 2 in left panel of figure 2). It is a consequence of the conical direction of synchrotron emission, and of the increment of optical depth (or average scattering number) by increasing L.

In general, for a given  $\theta_j$ , mean free path of photon  $\lambda$  and emission region size L, the fraction of photons exiting from the front face of the cylindrical emission region will decrease with decreasing R. Here, the unscattered synchrotron photons exiting from the front of the cylindrical region ( $SYN_{unsc}^{top}$ ) are those satisfying the condition  $z > L$  and  $\sqrt{x^2 + y^2} < 1.05R$  where (x,y,z) refer to spatial coordinate of photons with centre of the bottom face as the origin. Particularly, for 10% of total synchrotron photons, to exit unscattered from the front face the length of cylindrical region should be  $L = 5 \times 10^{-5}\lambda, 5 \times 10^{-4}\lambda, 5 \times 10^{-3}\lambda, \sim \lambda$  for  $R = 50L, 5L, 0.5L, 0.01L$  respectively (figure 2 right panel). Further, we notice that 100% unscattered photon can escape from the top (i.e.,  $SYN_{unsc}^{top} = 100\%$ ) when  $R > 0.1L$  while for  $R < 0.1L$   $SYN_{unsc}^{top}$  is always less than 100%, e.g., for  $R=0.01L$  the maximum  $SYN_{unsc}^{top}$  is 40% (as shown by curve 3 in right panel of figure 2).

#### 3.2 General properties of SED

As mentioned, in this section we are exploring the general properties of SED over issue, of limited energy range of synchrotron emission for calculating SSC (case 1), for subdominated random velocity components on IC spectra (case 2), and of dimension of emission region (case 3).

##### 3.2.1 Case 1

In general, emission in radio bands below a few 10s of GHz is dominated by the synchrotron-self absorption with emission from a much large region or multiple emission regions, contrary to the rapidly variable NIR to  $\gamma$ -ray emission – the focus of our study. However, neglecting radio emission below 10 GHz can affect the SSC as its the part of the seed photon for IC scattering. We, thus, investigated this effect on

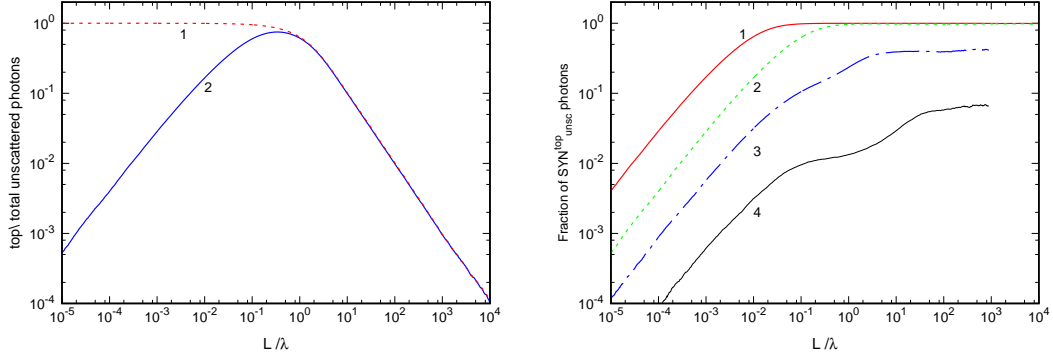


Figure 2: *Left*: Fraction of unscattered synchrotron photons to the total synchrotron photons for a jet apex angle  $\theta_j = 5^\circ$  and radius  $R = 0.5L$  as a function of length of the emission region in units of scattering mean free path. The solid curve represents the fraction of photons leaving from the face of the cylinder towards the observer while the dotted curve represents the fraction of total unscattered (top+sides) photons. *Right*: Fraction of unscattered synchrotron photons leaving from the front face of the cylindrical emission region for a fixed  $\theta_j = 5$  degree, but with different radius, here the curves 1, 2, 3 and 4 are for  $R = 5L, L/2, L/100$  and  $L/1000$  respectively.

spectral shape of the IC component by limiting the synchrotron minimum frequency  $\nu_{min}^{syn}$  at different values. For this we fixed  $\gamma_{min}$ , the peak frequency of synchrotron spectra  $\nu_p^{syn}$  and then compute the axial magnetic field strength  $B_o$  for known  $\nu_{min}^{syn}$  using  $\nu_{min}^{syn} = \frac{\gamma_{min}^2 \langle \gamma^{ran} \rangle^2}{1+z} \nu_B$ . We similarly compute the  $\gamma_b$  using equation (2) for a given  $\nu_p^{syn}$  and with the above estimated  $B_o$ . Figure 3a shows the SED for three values of  $\nu_{min}^{syn} = 10^{10}, 10^{11}, 10^{12}$  Hz (curves 1, 2, and 3 respectively) with  $\gamma_{min} = 100$ ,  $\nu_p^{syn} = 10^{14}$  Hz,  $\langle \gamma^{ran} \rangle = \frac{\gamma_{min}}{2} = 50$ . For all the three cases the spectra are similar, as expected, since the electrons energy distribution are almost same but the seed photons for SSC (synchrotron photons) are differed by  $\nu_{min}^{syn}$  values while the spectral index  $\alpha$  (where  $\alpha = (p-3)/2 = -0.45$ ,  $\nu^{syn} < 10^{14}$  Hz; and  $= (q-3)/2 = 0.55$ ,  $\nu^{syn} > 10^{14}$  Hz) is same. Also, the spectral index of SSC is similar to the spectral index of synchrotron emission, which is shown in figure 3a by plotting the dotted line at lower ( $\propto \nu^{0.45}$ ) and higher ( $\propto \nu^{-0.55}$ ) frequency end of SSC.

The curve 4 of figure 3a is a SSC spectra when the seed photon is a monochromatic photon of frequency  $8 \times 10^{13}$  Hz with other parameters being same. In this case also, the spectral index of SSC is similar to the spectral index of the synchrotron emission. Hence, the spectral index of SSC spectra is determined mainly by the electron energy distribution. Further, we see that when the monochromatic seed photon frequency is around  $\nu_p^{syn}$  ( $=10^{14}$  Hz) then the SSC spectral peak frequency is same to the case where seed photon has a broken power law with break frequency  $\nu_p^{syn}$  (e.g., curve 1 of figure 3a) but when it deviates much from  $\nu_p^{syn}$  the corresponding SSC spectral peak frequency also changes. Hence, the SSC spectral peak is mainly determined by the spectral synchrotron peak frequency  $\nu_p^{syn}$ .

For the three  $\nu_p^{syn}$  values mentioned above, the estimated  $B_o$  is 0.00014, 0.0014 and 0.014 gauss;  $\sqrt{\langle \gamma^2 \rangle}$  is 1146, 681 and 404;  $\gamma_b$  is 10000, 3162 and 1000 and  $\langle \gamma \rangle$  is 431, 357 and 277 respectively. Hence, the magnetic field strength determination by SED fitting is degenerate with  $\nu_{min}^{syn}$ , when  $\gamma_{min}$  and  $\nu_p^{syn}$  are fixed.

### 3.2.2 Case 2

Next we studied the arbitrariness and effect of the low magnitude random component of electrons velocity. We first compute the SED by varying  $\gamma_{min}^{ran}, \gamma_{max}^{ran}$  in such a way that  $\langle \gamma^{ran} \rangle$  ( $= \frac{\gamma_{min}^{ran} + \gamma_{max}^{ran}}{2}$ ) is fixed (shown in figure 3b) and also explored the effect by varying the  $\langle \gamma^{ran} \rangle$  (figure 3c). Curves labeled 1, 2 and 3 in figure 3b show the spectrum for a fixed  $\langle \gamma^{ran} \rangle \sim 50$ , but with  $\gamma_{min}^{ran} = 1.8, 10$  and  $49$ , and  $\gamma_{max}^{ran} = 100, 90$  and  $51$  respectively. As can be seen, the low end of the SSC spectra are affected. In general, the slope of the lower-end of spectra increase or spectra become harder with decreasing the separation between  $\gamma_{min}^{ran}$  and  $\gamma_{max}^{ran}$ , achieving maximum hardness for  $\gamma_{min}^{ran} = \gamma_{max}^{ran} = \langle \gamma^{ran} \rangle$ . The same hold for EC as well.

Figure 3c shows the SSC spectra for different  $\langle \gamma^{ran} \rangle$ . Curves 1, 2, and 3 correspond to  $\langle \gamma^{ran} \rangle$  of 2,



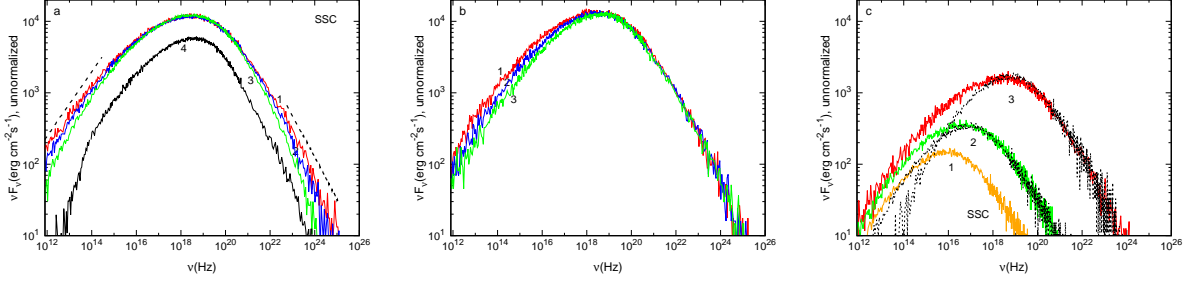


Figure 3: The general behavior of SED when the  $\nu_{min}^{syn}$  (or  $B_0$ ) varies (panel (a)) and when the random component of electrons velocity  $\gamma^{ran}$  varies (panel (b) and (c)). In panel (b), the range of  $\gamma^{ran}$  varies in such a way that average of  $\gamma^{ran}$ ,  $\langle \gamma^{ran} \rangle$ , is constant while in panel (c)  $\langle \gamma^{ran} \rangle$  also varies (see §3.2).

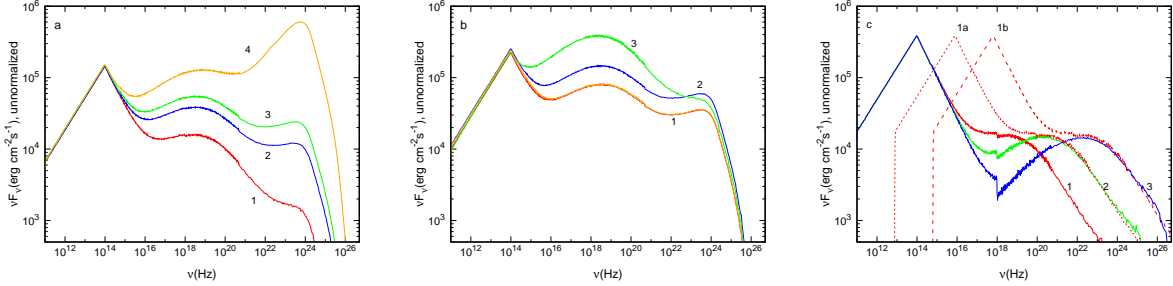


Figure 4: The general behavior of SED when  $L/\lambda$  varies for fixed  $R/L$  (panel (a)), when  $R/L$  varies for fixed  $L/\lambda$  (panel (b)), and when  $\gamma_{min}$  varies for fixed  $L/\lambda$ ,  $R/L$  (panel (c)). In panel (a), the curves 1, 2, 3, and 4 are for  $L/\lambda = 0.25, 0.5, 1$  and  $5$  respectively at  $R/L=0.5$ . In panel (b), the curves 1, 2 and 3 are for  $R/L = 0.5, 0.05$  and  $0.005$  respectively at  $L = \lambda$ . In panel (c), the curves 1, 2 and 3 are for  $\gamma_{min} = 100, 300$  and  $900$  and curves 1a and 1b are shifted curve 1 by factor  $3^4$  and  $9^4$  respectively.

6 and 51 with  $\gamma_{min}^{ran} = 1.8$  and  $\gamma_{max}^{ran} = 2, 10$  and  $100$  respectively. The peak of the curves 2 and 3 are shifted by a factor  $3^2$  and  $25.5^2$  with respect to peak of curve 1, shown by overplotting curve 1 using this factor. In general, for given parameter sets, the peak of the SSC/EC depends only on  $\langle \gamma^{ran} \rangle$  and not explicitly on  $\gamma_{min}^{ran}$ , or  $\gamma_{max}^{ran}$ . The slope of the lower-end of SSC/ EC spectrum, on the other hand, depends on  $\gamma_{min}^{ran}$  and  $\gamma_{max}^{ran}$  with maximum for  $\gamma_{min}^{ran} = \gamma_{max}^{ran} = \langle \gamma^{ran} \rangle$ .

### 3.2.3 Case 3

The other factor that affects the observed broadband spectrum is the dimension of the emission region. In the present case of cylindrical geometry, its primarily the ratio of radius to length,  $R/L$  and the ratio of length to the mean free path of the photons,  $L/\lambda$ . Figures 4a and 4b show the effect of  $L/\lambda$  and  $R/L$  on the SSC spectra. As expected, the average scattering number  $\langle N_{sc} \rangle$  increases with  $L$ , so the maximum emission of the SSC (photon counts corresponds to SSC peak) grows with  $L$  and for sufficiently large value of  $L$ , a Wien's peak starts to appear (curve 4 of figure 4a). Though it seems tempting that such peak may represent FSRQ SEDs, it corresponds to optically thick regime, inconsistent with observations. In  $L > \lambda$  limit, the ratio of emission at SSC peak to SYN peak increases with  $L$ , but is true only for  $R/L > 0.1$  since all unscattered photons escape from the top (front face of the cylinder). For  $R/L < 0.1$  case,  $SYN_{unsc}^{top}$  is less than 100 % and decreases with decreasing  $R/L$  (right panel of figure 2). Hence, in latter case, for a given  $R/L$  ( $< 0.1$ ) the ratio of emission at SSC peak to SYN peak remains almost constant for any  $L$  value.

Figure 4b shows the effect of variation of  $R$  for  $L = \lambda$  and here  $SYN_{unsc}^{top} = 97, 46$  and  $4.8$  % for the curves 1, 2 and 3 respectively. Effectively,  $\langle N_{sc} \rangle$  decreases with decreasing  $R/L$ , resulting in decrement of high SSC peak emission (which is appeared here around  $10^{24}$  Hz) and increment in ratio of emission at low SSC peak ( $\sim 10^{19}$  Hz) to SYN peak. Figure 4c shows the effect of variation of  $\gamma_{min}$  only, as was done in figure 3c. Here, curves 1, 2, and 3 are for  $\gamma_{min}$  (the square root of  $\langle \gamma^2 \rangle$ ) of 100 (681), 300

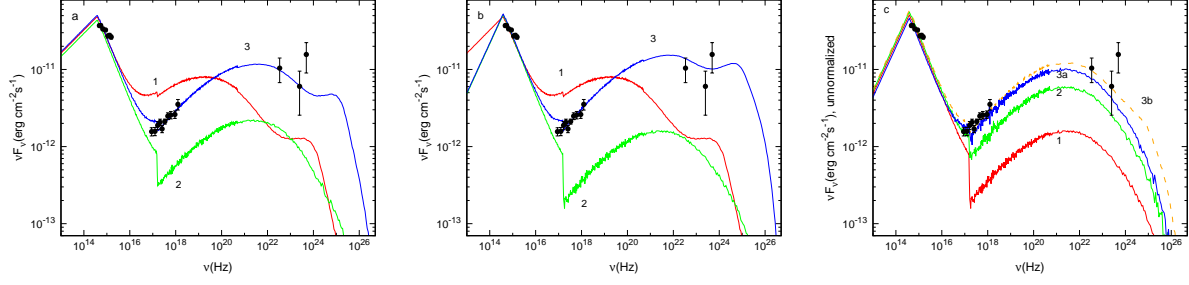


Figure 5: A Demonstration of SED modeling by SSC process only for  $CD < 1$ , the data points are for quiescent state of OJ 287 (Kushwaha et al. 2018a). In all three panels, the curve 1 is a starting/trial curve (except panel (c) where curve 1 is same as curve 2 of panel (b)). And curve 3 is a best modeled curve. The best modeled curve has been obtained in panel (a), (b), (c) by changing the combination of  $\gamma_{min}$  &  $L$ ;  $p$ ,  $\gamma_{min}$  &  $L$ ; and  $R/L$ ,  $p$ ,  $\gamma_{min}$  &  $L$  respectively.

(2045) and 900 (6137) respectively and correspondingly the SSC peak frequency [ $\nu_p^{SSC} \propto \langle \gamma^{ran} \rangle^2 \langle \gamma^2 \rangle^2 \nu_B$ ] of the curves 2 and 3 increases by factor  $9^2$  and  $81^2$  with respect to the SSC peak frequency of the curve 1. Here, we like to stress that in our model the SSC peak is degenerate over  $\langle \gamma^{ran} \rangle$  and  $\gamma_{min}$  (or the square root of  $\langle \gamma^2 \rangle$ , or  $\langle \gamma \rangle$ ). The same SSC peak frequency can be modelled for lower  $\langle \gamma^{ran} \rangle$  and correspondingly higher  $\gamma_{min}$  (or higher anisotropy in electron motion).

### 3.3 SED fitting Demonstration

Blazar characteristic broad double-humped SED is categorized primarily by the frequency at which synchrotron emission peaks, and the ratio of luminosities at high-energy hump peak to synchrotron peak in  $\nu F_\nu$  representation; generally referred in the literature as ‘‘Compton dominance’’ (CD) (e.g., Dermer & Giebels 2016). Here, we introduce a general way of SED modeling considering SSC for two cases, based on the Compton dominance. Case-I considers blazars with  $CD < 1$  while Case-II with  $CD \gtrsim 1$ . In general, the X-ray spectrum in case-II is comparatively harder than the case-I. As shown in the previous section, the peak of SSC/EC depends only on  $\langle \gamma^{ran} \rangle$  while the slope of the low-energy end of SSC/EC spectrum depends on  $\gamma_{min}^{ran}$  and  $\gamma_{max}^{ran}$  with slope achieving maximum for  $\gamma_{min}^{ran} \approx \gamma_{max}^{ran} = \langle \gamma^{ran} \rangle$  and minimum for  $\gamma_{min}^{ran} \ll \gamma_{max}^{ran} \approx 2\langle \gamma^{ran} \rangle$ . So for SED modeling in the Case-II, we assumed  $\gamma_{min}^{ran} \approx \gamma_{max}^{ran} = \langle \gamma^{ran} \rangle$  while  $\gamma_{min}^{ran} = 1.8$ ,  $\gamma_{max}^{ran} = \gamma_{min}$  for Case-I. Below, we demonstrate our approach without bothering about the fairness of parameters vis-a-vis observations.

#### 3.3.1 Case-I SED

Figure 5 demonstrates the SED modeling by SSC process for case-I. We have chosen the observation ID of source OJ 287 (from Kushwaha et al. 2018a) where  $CD \approx 1/4$ . We have attempted to model the SED in three different ways (as shown in figure 5 (a),(b),(c)) exploiting the degeneracies between parameters. For all the cases, the starting parameters set is  $\gamma_{min} = 100$  and  $L = 1.1 \times 10^{14} \text{ cm} = 0.35\lambda$ ,  $p = 2.4$ ,  $R/L = 0.5$ ;  $q = 4.5$ ,  $\gamma_{max} = 40000 = 20\gamma_b$ ,  $\langle \gamma \rangle = 260$ ,  $B_o = 0.014$  gauss,  $\theta_j = 10$  degree,  $n_e = 10^{14} \text{ cm}^{-3}$  (here  $\langle \gamma \rangle / \langle \gamma^{ran} \rangle = 5.2$ , meant an anisotropic flow), the corresponding spectrum is shown by curve 1 in panel (a) and (b), as a trial or guess values. In which the SSC peak is around  $10^{19}$  Hz and the intensity of minimum X-ray frequency is higher than the observed one. To decrease the intensity at the lower-end of X-ray spectrum and increase the SSC peak frequency from curve 1, in panel (a), we had increased the  $\gamma_{min}$  to 350 (shown by curve 2). In panel (b) we had decreased the  $p$  to 1.7 and increased the  $\gamma_{min}$  to 250 (shown by curve 2), resulting in a shift of SSC peak frequency to  $10^{21}$  Hz. The best model description are shown by curve 3 in panels (a) and (b), where  $\gamma$ -ray peak intensity is matched by increasing the size of region (results in  $\langle N_{sc} \rangle$  increment) with  $L = 2.45 \times 10^{15}$ ,  $7.52 \times 10^{15}$  cm for panel (a) and (b) respectively.

In panel (c), we start with the curve 2 of panel (b) but now to increase the ratio of  $\gamma$ -ray peak to synchrotron peak intensity (as shown in figure 4b) we decreased the  $R/L$  to 0.1 (curve 2) and to 0.03 (curve 3a, which is also a best modeled curve with  $L = 1.1 \times 10^{14}$  cm). And the another best model

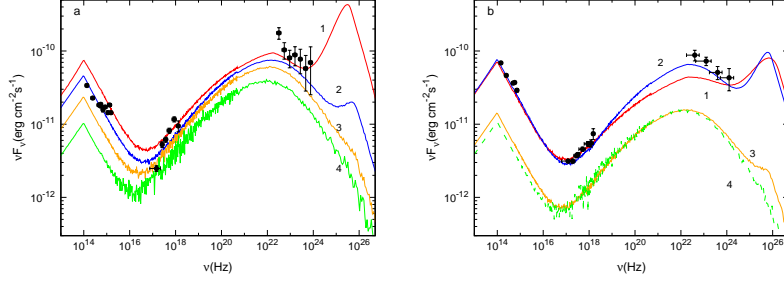


Figure 6: A Demonstration of SED modeling by SSC process only for  $CD \gtrsim 1$ . The panel (a) is for quiescent phase of 3C 454.3 (Shah et al. 2017) and (b) is for flaring phase of OJ 287 (Kushwaha et al. 2013), here all curves of both panels are best modeled one which is obtained mainly by varying R/L. In panel (a) the curves 3 and 4 are lowered by factor 2 and 4 respectively and in panel (b) the curves 3 and 4 both are lowered by factor 5.

description curve 3b has been obtained from curve 2 by increasing L to  $1.1 \times 10^{15}$  cm.  $\langle N_{sc} \rangle$  for best model description curve of panels (a), (b) and (c) (curves 3a and 3b) are 1.12, 1.25, 1.003 and 1.04, and  $SYN_{unsc}^{top}$  is 98, 98, 1.1 and 20 % respectively. In short, we have modeled the same data in 3 different way using degeneracy between parameters as discussed in the previous subsections. In first approach, we changed only  $\gamma_{min}$  and L while in second, we decreased the spectral index  $p$  and comparatively lowered  $\gamma_{min}$  but with a higher L than the first approach. We also found that of all, in third approach, by changing R/L which leads to lowest L.

### 3.3.2 Case-II SED

Next we demonstrate the SED fitting by SSC only for case-II. For this, we have selected two observation IDs, a quiescent phase of 3C 454.3 (FSRQ, Shah et al. 2017) and a flaring state of OJ 287 (BL Lacs object, Kushwaha et al. 2013). CD is  $\sim 2$  and  $\sim 1$ , shown respectively in figure 6a and 6b. For SED modeling, we have used the random component of electron  $\gamma_{min}^{ran} \approx \gamma_{max}^{ran} = \langle \gamma^{ran} \rangle$  for panel (a), and  $\gamma_{min}^{ran} = 1.8$ ,  $\gamma_{max}^{ran} = \gamma_{min}$  for panel (b). For  $\gamma$ -ray dominated emission, the model requires either a large average scattering (or  $L/\lambda > 1$ , so top-uns scattered SYN photon will be less), or small R/L value (so again top-uns scattered SYN photon will be less, see figure 4b). Mainly, we have attempted by decreasing R/L value in order to get a small average scattering number. Since in large scattering limit, we will see Wien peak like features (shown by curve 1 and 2 in both panels of figure 6) and also one can not avoid the pair-production over IC process. To best of our knowledge, none of the observed SED had reported Wien peak feature seen in the model curves at the high energy ends.

In both panels 6a and 6b, all curves are best description to the data points except that some are shifted down from the data points for clarity. Here, curves 1, 2, 3 of figure 6a and 2, 3, 4 of figure 6b are for R/L = 0.05, 0.005, 0.0005 respectively while R/L = 0.00005 for curve 4 (in figure 6a) and R/L = 0.5 for curve 1 (in figure 6b). L values for figure 6a curves 1, 2, 3 and 4 are  $1.0 \times 10^{17}$  ( $\sim 4\lambda$ ),  $2.8 \times 10^{16}$  ( $\sim 0.6\lambda$ ),  $1.8 \times 10^{16}$  ( $\sim 0.4\lambda$ ) and  $1.8 \times 10^{16}$  ( $\sim 0.4\lambda$ ) cm,  $SYN_{unsc}^{top}$  is 69, 4, 0.3 and 0.03 %, and  $\langle N_{sc} \rangle$  is 2.04, 1.06, 1.007 and 1.001 respectively. Similarly, L values for curves 1, 2, 3, and 4 of figure 6b are  $1.3 \times 10^{17}$  ( $\sim 1.9\lambda$ ),  $7.9 \times 10^{16}$  ( $\sim 1.5\lambda$ ),  $1.3 \times 10^{16}$  ( $\sim 0.25\lambda$ ) and  $5.3 \times 10^{15}$  ( $\sim 0.1\lambda$ ) cm; and  $SYN_{unsc}^{top}$  is 99, 55, 2.5 and 0.14 % and  $\langle N_{sc} \rangle$  is 1.55, 1.37, 1.02 and 1.002 respectively. In short, to model the Compton dominated SEDs in single scattering limit in SSC process, the lowest R/L value ( $< 0.01$ ) is more preferable. In both cases of SED modeling demonstration, we have fixed an electron density,  $n_e = 10^{14} \text{ cm}^{-3}$  which correspond to the mean free path  $\lambda = 4 \times 10^{14} \text{ cm}$  for  $\langle \gamma \rangle = 260$ . Here, we like to stress that for a comparatively smaller  $n_e$  ( $\sim 10^8 \text{ cm}^{-3}$ ) the size L (for same SEDs) will become an order of 100 pc, as now  $\lambda = 4 \times 10^{20} \text{ cm}$  with same  $\langle \gamma \rangle$ . In this extreme case, one can not assume a cylindrical emission region, and in SED calculations one have to take an account of the density variation with length L, since for conical region the density decreases by square of the radius of cross section.

## 4 SED Comparison and Discussions

We performed a comparative study of blazars SED modeling from a local relativistic anisotropic flow in a conical jet scenario and explored the physical parameters space. We modeled five different SEDs of blazars, three for BL Lac object, one each for OJ 287 ( $z = 0.306$ ), S5 0716+714 ( $z = 0.31$ ) and PKS 2155-304 ( $z = 0.116$ ), and the rest two for FSRQ 3C 454.3 ( $z = 0.859$ ). The BLL OJ 287 has exhibited diverse spectral phases, from LBL (Kushwaha et al. 2013) to LBL+HBL (Kushwaha et al. 2018b,a). For BLLs broadband SEDs, we have taken LBL phase of OJ 287, IBL S5 0716+714 (from Chandra et al. 2015), and HBL PKS 2155-304 (from Gaur et al. 2017, epoch 2012). For FSRQ, we have selected a quiescent and a flaring phase of 3C 454.3 from Shah et al. (2017). In our conical jet model for a given  $\gamma$ -ray flare time scale ( $t_{var}$ ) the emission region size  $L$  can be estimated as,

$$L \leq \frac{ct_{var}}{1+z}. \quad (4)$$

We defined,  $L^\circ = ct_{var}/(1+z)$  as a maximal observable emission size. For flaring phase of 3C 454.3, Shah et al. (2017) have reported a 10 hours  $\gamma$ -ray variability, so  $L \leq 5 \times 10^{14}$  cm. In general, for FSRQ SEDs, in addition generally to agreed EC scenario, we have also attempted to model the SED by SSC only. For BLLs, however, we have considered SSC only. For all four sources, we consider an average semi-aperture angle  $\theta_j \sim 5$  degree (like, Ghisellini & Tavecchio 2009). In section §3.2, we have shown that the magnetic field strength is degenerate with  $\nu_{min}^{syn}$  for fixed  $\gamma_{min}$  and  $\nu_p^{syn}$  for given SED. We have computed the magnetic field strength  $B_o$  by fixing the  $\nu_{min}^{syn}$  as,  $\nu_{min}^{syn} = \frac{\gamma_{min}^4}{4(1+z)}\nu_B$ , here  $\gamma^{ran} = \gamma_{min}/2$  (e.g., see equation (2)). Like previous section, we fix the electron density  $n_e^* = 10^{16}$  cm $^{-3}$  for all Obs. ID, this will provide a trial  $L$  to start with. Later, we make this  $L$  to order of  $L^\circ$  by adjusting (increasing or decreasing) the  $n_e^*$  by factor  $a$  as,  $n_e = a n_e^*$ ; where  $a = L / L^\circ$ . Since, in IC process the spectrum depends on average number scattering  $\langle N_{sc} \rangle$ , it degenerates over  $n_e$  (or  $\lambda$ ) and  $L$ . Mainly, we are estimating the electron density for given observed SEDs and its variability time scale (or  $L^\circ$ ). In additions, the model curves are well describe the observed data points, when it is computed in single scattering limits,  $\langle N_{sc} \rangle \sim 1$  (i.e., optically thin medium).

### 4.1 Considering both SSC and EC

The broadband SEDs of FSRQs are usually modeled by SYN, SSC, and EC with EC component dominating over SSC in general. The generally invoked seed photon source for EC is torus (IR) and broad line region (BLR). Here, we considered these two, described by a blackbody profile with temperature corresponding to the frequency at which their emission peaks. The temperature for torus is  $\leq 1800$  K while BLR is  $\sim 40000$  K. We have chosen two temperature values ( $T_{EC}$ ), 500 and 50k K to extract a general picture in order to understand which describes the data better assuming simply an isotropic distribution of seed photons inside the medium.

Figures 7 and 8 show modeling of a flaring and a quiescent phase of FSRQ 3C 454.3. In both the figures, the left and right panels are for 500 and 50k K with panels (a), (b), (c) corresponding to  $SYN_{unsc}^{top}$  of  $\sim 100$ , 10 and 1 % respectively, computed simply by decreasing  $L$  while rest parameters (as shown in table 1) being fixed. As discussed in section §3.1 the  $SYN_{unsc}^{top}$  is 100, 10 and 1 % for  $L/\lambda = 0.03$ ,  $5.1 \times 10^{-4}$ ,  $2.9 \times 10^{-5}$  at  $R/L = 5$ ; and  $= 0.3$ ,  $5.1 \times 10^{-3}$ ,  $2.9 \times 10^{-4}$  at  $R/L = 0.5$  respectively,  $L$  is decreasing from panel (a) to (c). The solid curve is for  $R/L = 0.5$  and dotted curve is for  $R/L = 5$  with same parameters. Both curves are almost identical, since we are changing only geometry parameters  $R$  and  $L$  in such a way that  $SYN_{unsc}^{top}$  is constant, and as their ratio  $R/L$  is greater than 0.1 so average scattering number  $\langle N_{sc} \rangle$  is also similar. When  $R < 0.1L$ , as discussed in previous section,  $SYN_{unsc}^{top}$  never reaches 100% and the difference in SSC/EC spectra is sent to appear. In figure 9 we have modeled the quiescent and flaring phase of 3C 454.3 for  $R/L = 0.01$  which corresponds to  $SYN_{unsc}^{top} \sim 1\%$ .

We find that a wide range of seed photon temperature for EC (500 – 50k K) capable of describing the SEDs well for both flaring and quiescent states. Only when  $R/L < 0.1$ , model fails to describe SEDs (as shown in figure 9). Particularly, for high temperature 50k K, the model fails to describe the SED for same  $p$  values (2.1) of that of the low temperature (500 K). The modeled SED is shown by three different particle spectral indices  $p$  values 1.4, 1.8 and 2.1 (curve 1, 2 and 3 respectively in right panel of figure 7a) with lowest one ( $p=1.4$ ) being the best description.

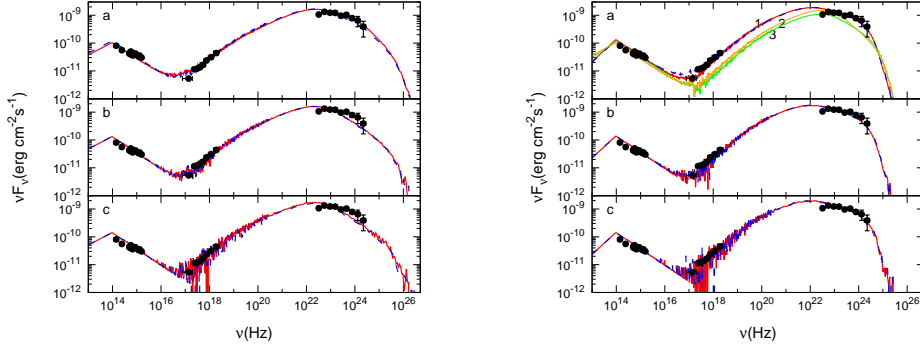


Figure 7: SSC+EC explanation of high energy emission of flaring phase of 3C 454.3 (Shah et al. 2017). The EC blackbody temperature is 500 and 50k K for left and right panel respectively. The panels (a), (b) and (c) are for  $SYN_{unsc}^{top}$  100, 10, 1 % respectively, computed simply by decreasing L from (a) to (c) (see §3.1). The curves are total emission under synchrotron, SSC and EC explanation in which the dotted curve is for  $R/L = 5$  and solid curve is for  $R/L = 0.5$ .

Table 1: Spectral free parameters for SED modeling (SYN+SSC+EC) of FSRQ 3C 454.3 as shown in figures 7- 9.  $n_e$  is estimated as,  $n_e = a n_e^*$ ; where,  $a = L/L^o$ ,  $L^o \sim 5 \times 10^{14}$  cm, and L is computed for  $n_e^* = 10^{16}$   $\text{cm}^{-3}$  (see text for details).

	figure 7 (flaring)				figure 8		figure 9		figure 9	
	(a) <sub>l</sub>	(a) <sub>r</sub> , for curves			(quiescent)		(quiescent)		(flaring)	
		1	2	3	(a) <sub>l</sub>	(a) <sub>r</sub>	(a) <sub>S</sub>	(a) <sub>D</sub>	(b) <sub>S</sub>	(b) <sub>D</sub>
$\langle N_{sc} \rangle$	1.05	1.03	1.03	1.03	1.05	1.04	1.0	1.0	1.0	1.0
$\lambda$ ( $10^{16}$ cm)	13.0	0.18	0.26	0.18	1.3	0.016	5.9	0.031	48.0	0.76
$L\#$ ( $10^{14}$ cm)	39.0	0.54	0.78	0.54	3.9	0.048	10.1	0.043	86.4	1.0
$B_o\#\#$ (G)	2.1e-4	1.0e-2	2.2e-2	1.6e-2	2.1e-3	1.7e-1	4.9e-4	1.0e-1	6.1e-5	2.2e-2
$T_{EC}$ (K)	500	50k	50k	50k	500	50k	500	50k	500	50k
$\langle \gamma \rangle^{**}$	604	321	270	207	340	113	491	132	831	459
$\gamma_b^{**}$	6900	1509	2156	2372	3881	1293	5606	1509	9488	2156
$\gamma_{min}^{**}$	160	35	50	55	90	30	130	35	220	50
$p$	2.1	1.4	1.8	2.1	2.1	2.1	2.1	2.1	2.1	1.4
$q$	4.1	4.1	4.1	4.1	4.1	4.1	4.1	4.1	4.1	4.1
R/L	5***	5***	5***	5***	5***	5***	0.01	0.01	0.01	0.01

\*\* in units of  $m_e c^2$ ; \*\*\*  $\sim 100\%$  unscattered synchrotron photons escape from top of the emission region

#  $L = 5.1 \times 10^{-4}$ ,  $2.9 \times 10^{-5} \lambda$  for  $SYN_{unsc}^{top} = 10, 1\%$  when  $R/L = 5$  and so on (see text).

##  $B_o$  has been computed for fixed  $\nu_{min}^{syn}$  as,  $\nu_{min}^{syn} = \frac{\gamma_{min}^4}{4(1+z)} \nu_B$ .

l: left; r: right panels of respective figure; and S: solid; D: dashed curve in figure 9

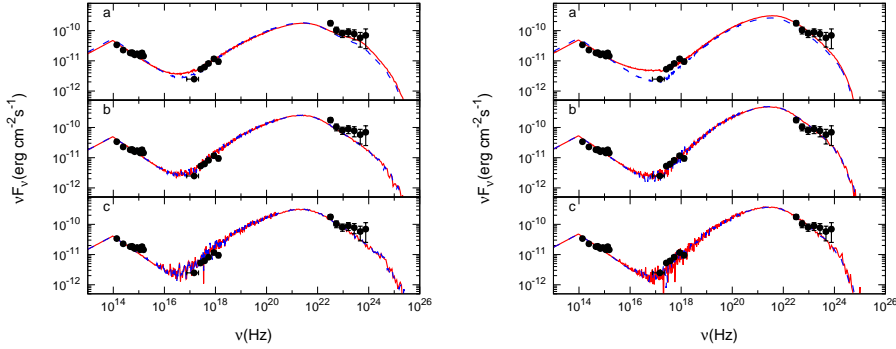


Figure 8: SSC+EC explanation of high energy emission of quiescent phase of 3C 454.3 (Shah et al. 2017), the rest is same as in figure 7.

The estimated size  $L$  for  $T_{EC} = 500$  K is  $\sim 3.9 \times 10^{12}$ ,  $3.9 \times 10^{13}$  cm at  $\text{SYN}_{unsc}^{top} = 1\%$  (shown in left panel of figure 7c, where  $\lambda = 1.3 \times 10^{17}$  cm for  $n_e = 10^{16}$   $\text{cm}^{-3}$ , listed in table 1), and at  $\text{SYN}_{unsc}^{top} = 10\%$ ,  $L = 6.6 \times 10^{13}$ ,  $6.6 \times 10^{14}$  cm for  $R = 5L$ ,  $0.5L$  respectively. But if we decrease  $n_e$  by factor 100, i.e.,  $n_e = 10^{14}$   $\text{cm}^{-3}$  then  $\lambda$  will increase with same factor,  $\lambda = 1.3 \times 10^{19}$  cm so the estimated  $L$  is now order of  $10^{14}$  cm or order of the  $\gamma$ -ray variability for  $R/L = 5$  at  $\text{SYN}_{unsc}^{top} = 1\%$ . Similarly, for  $\text{SYN}_{unsc}^{top} = 10, 100\%$ , with having  $n_e \approx 2 \times 10^{15}$ ,  $10^{17}$   $\text{cm}^{-3}$  respectively for  $R/L = 5$ , we can explain the observed  $\gamma$ -ray variability. And for  $T_{EC} = 50$  K, the minimum electron density (i.e., for  $\text{SYN}_{unsc}^{top} = 1\%$ ) for explaining the  $\gamma$ -ray variability is  $\sim 10^{12}$   $\text{cm}^{-3}$ . Hence to explain the 10 hours  $\gamma$ -ray variability of this Obs. ID. of flaring phase in this model, the electron density must be greater than  $10^{12}$   $\text{cm}^{-3}$  but the better constraint on  $n_e$  will come if one can estimate observationally the fraction of synchrotron photons which escape from the side of the emission region (i.e., the fraction of off-axis synchrotron emission), and better constraint on  $T_{EC}$ .

Since broadband modeling allows us to constrain the contribution of SSC and EC flux in total observed flux and thus, the seed photon density for SSC (i.e.,  $n_e$ ), one can estimate the seed photon density for EC. The estimated range is  $\sim (15 - 135) n_e$  for flaring and  $\sim (5 - 60) n_e$  for quiescent phase. For both phases, we are almost in single scattering limit, e.g., the  $\langle N_{sc} \rangle$  vary from 1.10 to 1.001 for panel (a)-(c) in left panel of figure 7. The same is the case for the quiescent phase SED as well. The single scattering limit is also the reason for our calculations not being affected from the pair-production as discussed previously. Shah et al. (2017) had modeled the above SED in one-zone model where the  $\gamma_b$  is associated with peak of the two humps. On the contrary, in our continuous-jet case mainly  $\langle \gamma^2 \rangle$  (as,  $\nu_p^{SSC} \approx \langle \gamma^{ran} \rangle^2 \langle \gamma^2 \rangle^2 \nu_B$ ) determines the  $\gamma$ -ray peak. For flaring and quiescent states,  $\gamma_b$  is 2500 and 1800 in Shah et al. (2017) while  $\sqrt{\langle \gamma^2 \rangle}$  is 1255, 706 in our continuous-jet case (for 500K seed photon field only), comparatively lesser than one-zone model values. The high energy peak of modeled spectra for flaring and quiescent phase occur at  $\sim 4 \times 10^{22}$ , and  $4 \times 10^{21}$  Hz respectively and corresponding  $\gamma_b$  is 6900 and 3881 respectively (as shown in table 1, here for both cases we fixed the same synchrotron peak frequency  $\nu_p^{syn} = 1.86 \times 10^{14}$  Hz), hence our model is consistent with the observational fact that for high  $\gamma$ -ray peak we have higher synchrotron peak, which we have explicitly discussed in section §3.2 (see figure 3a). In all cases (listed in table 1), the anisotropic flow is maintained as the average forward velocity component  $\langle \gamma \rangle$  is almost more than 7 times larger to the average random velocity component  $\langle \gamma^{ran} \rangle$  ( $\approx \gamma_{min}/2$ ).

## 4.2 Only SSC for BLLs SEDs

In our systematic study, we also explored the parameter space to study the feasibility of SSC in reproducing high energy emission of the LSP class of SEDs for both BLLs and FSRQs. It was based on our demonstration in the previous section that SEDs with  $CD > 1$  can be fitted by decreasing the  $R/L$  value. A modeled SED for BLLs OJ 287 (LBL), S5 0716+714 (IBL) and PKS 2155-304 (HBL) are shown in left, middle and right panel of figure 10 respectively and FSRQ 3C 454.3 is shown in figure 11 with the corresponding model parameters in the table 2 and 3.

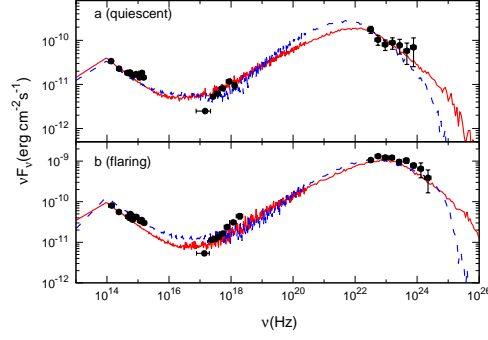


Figure 9: SSC+EC explanation of high energy emission of quiescent (upper row) flaring (lower row) phase of 3C 454.3 (Shah et al. 2017). In both panel,  $SYN_{unsc}^{top} = 1\%$ ,  $R/L = 0.01$ ; and  $T_{EC} = 500, 50k$  K for solid and dotted curve respectively.

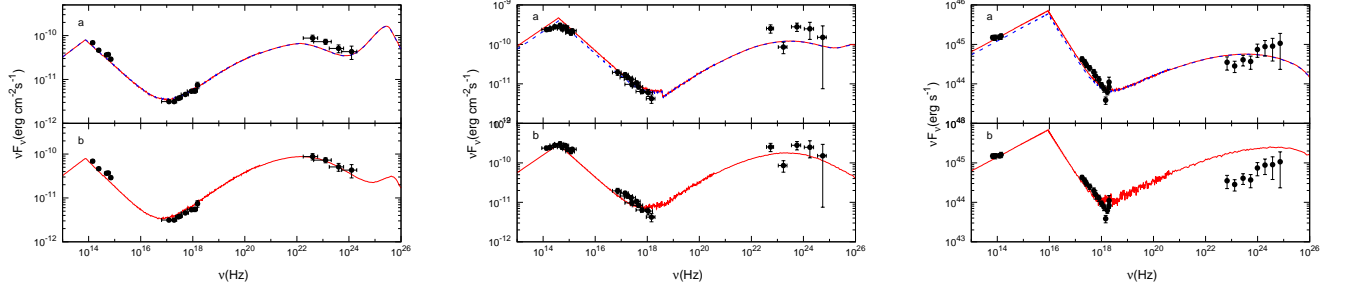


Figure 10: SSC explanation of high energy emission of LBL OJ 287 (Kushwaha et al. 2013), IBL S5 0716+714 (Chandra et al. 2015), and HBL PKS 2155-304 (Gaur et al. 2017). The left panel corresponds to a flaring SED of OJ 287 the middle and right panels correspond to the IBL and HBL respectively. The curves are total emission under synchrotron and SSC explanation (see §4.2).

Table 2: Spectral free parameters for SED modeling (SYN+SSC) of BLLs OJ 287 (LBL), S5 0716+714 (IBL) and PKS 2155-304 (HBL) which is shown in figure 10. Here, l: left; m: middle; r: right panels of figure 10;  $L^\circ \sim 2 \times 10^{15}$  cm for all SEDs; rest is same as in table 1.

	LBL		IBL		HBL	
	(a) <sub>l</sub>	(b) <sub>l</sub>	(a) <sub>m</sub>	(b) <sub>m</sub>	(a) <sub>r</sub>	(b) <sub>r</sub>
$\langle N_{sc} \rangle$	1.61	1.08	1.16	1.01	1.05	1.00
$L$ ( $10^{14}$ cm)	5.0	2.1	5.6	0.86	0.81	0.31
$\lambda$ ( $10^{14}$ cm)	2.1	3.6	8.5	8.5	3.5	13.0
$B_o^{###}$ (G)	4.7e-6	1.6e-6	8.1e-7	8.1e-7	4.4e-6	3.2e-7
$\langle \gamma \rangle^{**}$	1924	2507	3828	3828	2464	4764
$\gamma_b^{**}$	8391	10973	25714	25714	75000	145000
$\gamma_{min}^{**}$	650	850	1150	1150	750	1450
$p$	2.1	2.1	2.1	2.1	2.3	2.3
$q$	4.1	4.1	4.1	4.1	5.1	5.1
R/L	5	0.01	5	0.01	5	0.01
$SYN_{unsc}^{top}$ (%)	100	8	100	3	100	1

In figure 10, the solid and dashed curves in panel (a) represent the model flux for R/L = 5 and 0.5 respectively while the bottom panel (b) corresponds to R/L = 0.01. As discussed in previous section, here also the model SED is almost identical for R/L = 5 and 0.5. In LBL and IBL case, CD is  $\sim 1$ . We find, the best described model SED is obtained at R/L < 0.01. Typically in both sources the  $\gamma$ -ray variability time scale is order of few days (e.g., Goyal et al. 2018; Chandra et al. 2015). The reported 2 days variability constrains the emission region size  $L \lesssim 2 \times 10^{15}$  cm.

For R/L = 0.01, the model computed L is  $2.1 \times 10^{14}$  and  $8.6 \times 10^{13}$  cm for OJ 287 and S5 0716+714 respectively (as listed in table 2), at  $n_e = 10^{16} \text{ cm}^{-3}$ . Like previously, we used the existed degeneracy between parameters  $n_e$ ,  $\lambda$ , and L (in SED modeling) to make L order of variability time scale. For this we decrease  $n_e$  almost by one order, i.e.,  $n_e = 10^{15} \text{ cm}^{-3}$ . The estimated  $n_e$  is very large and seems unphysical. But we like to stress that it is a required density to generate the statistically significant SSC spectra in single scattering limit ( $\langle N_{sc} \rangle \sim 1$ ). Hence 2 days  $\gamma$ -ray variability of OJ 287 and S5 0716+714 can be explained with electron number density  $\sim 10^{15} \text{ cm}^{-3}$  at R/L = 0.01 and  $\langle \gamma^{ran} \rangle \sim \gamma_{min}/2$ . Since we are explaining the SED for R/L < 0.1 where  $SYN_{unsc}^{top}$  never become 100%, we also expect the emission from the side of the jet emission region or off-axis jet emission. As mentioned earlier, the SSC peak frequency is degenerate over  $\langle \gamma^{ran} \rangle$  and  $\langle \gamma^2 \rangle$ , we can model the same SED with increasing the anisotropy of electron motions ( $\langle \gamma \rangle$ ). But, we need a larger electron density, to make the emission region size order of variability time scale, as the mean free path  $\lambda$  increases with  $\langle \gamma \rangle$  for given  $n_e$ . In general, to explain the observed  $\gamma$ -ray variability of given SEDs, the required electron density will increase with increasing the anisotropy of electron motions. For HBL PKS 2155-304, we have model spectra with CD < 1. We find that for R/L > 0.01, the model SSC spectra explain the observation well with size  $L \sim 8.1 \times 10^{13} \text{ cm}$  at  $n_e = 10^{16} \text{ cm}^{-3}$ . Similarly, to explain the two days  $\gamma$ -ray variability for PKS 2155-304, the electron density should be order of  $10^{15} \text{ cm}^{-3}$ .

### 4.3 Only SSC for FSRQ SEDs

In figure 11, the left and right panel show a quiescent and flaring state SED of FSRQ 3C 454.3 from Shah et al. (2017) respectively. For the quiescent state, the solid and dashed curves in panel (a) represent the model flux for R/L = 5 and 0.5 respectively while the bottom panel (b) represents model flux for R/L = 0.01. For the flaring state, the model SSC flux is computed for R/L = 0.01 (upper panel) and 0.0001 (bottom panel) and the corresponding size  $L = 8.3 \times 10^{15} \text{ cm}$  and  $= 3.3 \times 10^{15} \text{ cm}$  respectively at  $n_e = 10^{16} \text{ cm}^{-3}$  (as listed in table 3). In single scattering limit, R/L < 0.01 is preferred for both flaring and quiescent phase. To explain 10 hours  $\gamma$ -ray variability ( $L \leq 5 \times 10^{14} \text{ cm}$ ), the electron number density should be order of  $10^{17} \text{ cm}^{-3}$ , which is very large density even two order greater than estimated BLLs electron density and  $\sim 4$ -5 order greater than EC dominated case. Here we like to stress that in same analogy one can explain one second  $\gamma$ -ray variability with electron density  $\sim 10^{22} \text{ cm}^{-3}$  for this SED. Broadly, we can produce the observed FSRQ SEDs with SYN+SSC consideration, having a very large electron density (even comparable to the electron density of the inner disk region). However, in subsection 4.5 we show that in this case the total electrons of the emission region is  $\sim 9$  orders lesser than the inner disk region. That is, the jet matters have been supplied by the inner disk region and jet matter density get increased due to a small R/L. Thus, the observed FSRQ SEDs can also be described well with SYN+SSC consideration.

### 4.4 Jet Power

The kinetic energy of the jet in leptonic case (here it is assumed that the hadrons are cold and do not participate in the radiative process, so they do not contribute to jet mechanical power significantly) for conical jet model is (e.g. Zdziarski 2014)

$$P_{jet} = \dot{M}c^2 [\langle \gamma^R \rangle + (\gamma^B - 1)] \quad (5)$$

Here  $\langle \gamma^R \rangle = \langle \gamma \rangle \langle \gamma^{ran} \rangle$ ,  $\dot{M}$  is a mass outflow rate of jet,  $\dot{M} = \pi R^2 n_e m_e \beta c$ , R is the cross-section of the jet (or radius of the cylindrical emission region),  $\beta = \sqrt{1 - \frac{1}{\langle \gamma \rangle^2}}$  is the outflowing velocity component of the electrons,  $\gamma^B = \left( \sqrt{1 - \frac{v_A^2}{c^2}} \right)^{-1}$ ,  $v_A = B_o / \sqrt{4\pi n_e m_e}$  is the Alfven velocity of the electrons. In above equation (5), the first term represents the outflowing component and the last term is the magnetic



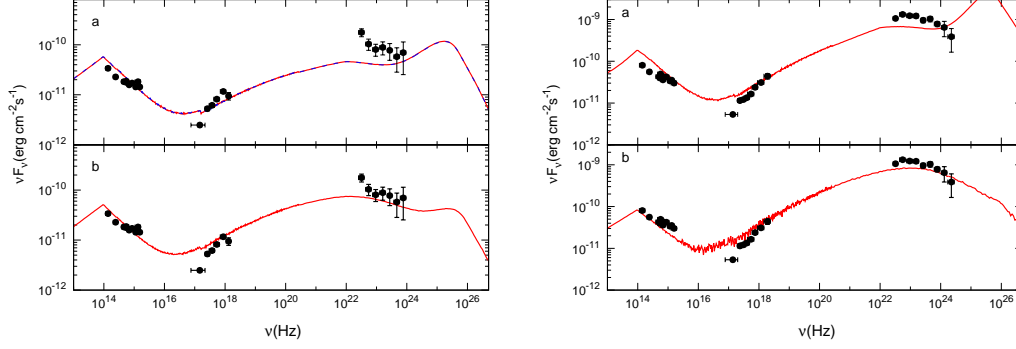


Figure 11: Quiescent (left) and flaring (right) state SED of 3C 454.3 from (Shah et al. 2017). The curves are the total emission assuming synchrotron and SSC processes (see §4.3).

Table 3: Spectral free parameters for SED modeling (SYN+SSC) of FSRQ 3C 454.3 as shown in figure 11. Here, l: left; r: right panels of figure 11; rest is same as in table 1.

	(a) <sub>l</sub>	(b) <sub>l</sub>	(a) <sub>r</sub>	(b) <sub>r</sub>
$\langle N_{sc} \rangle$	1.77	1.16	2.8	1.00
L ( $10^{14}$ cm)	9.8	6.3	83.0	33.0
$\lambda$ ( $10^{14}$ cm)	3.5	5.9	7.5	16.0
$B_o^{\#\#}$ (G)	7.9e-7	2.7e-7	1.7e-7	3.6e-8
$\langle \gamma \rangle^{**}$	2455	3211	3589	5289
$\gamma_b^{**}$	28033	36658	40971	60378
$\gamma_{min}^{**}$	650	850	950	1400
$p$	2.1	2.1	2.1	2.1
$q$	4.1	4.1	4.1	4.1
R/L	5	0.01	0.01	0.0001
$SYN_{unsc}^{top}$ (%)	100	10	25	0.1

field. For chosen set of parameters, the estimated magnetic field suggest that the Alfvén speed is non-relativistic. Hence in presented formalism, the jet is a matter dominated not a poynting flux (e.g., [Sikora et al. 2005](#)). In addition, the contribution of hadrons in the jet power is negligible as the average Lorentz factor of electron  $\langle\gamma^R\rangle$  is always greater than 5500 and hadrons are non-relativistic (cold).

We estimated the jet power for best modeled SED of all sources.  $P_{jet}$  is  $\sim 2.7 \times 10^{51}$  and  $7.0 \times 10^{49}$  erg/s for EC dominated (right panel of figure 7c) and SSC only (right panel of figure 11b) case of flaring state of 3C 454.3 respectively. For BLL the jet power of best modeled SED for OJ 287 (left panel of figure 10b), S5 0716+714 (middle panel of figure 10b) and PKS 2155-304 (right panel of figure 10a) are  $\sim 3.3 \times 10^{52}$ ,  $6.8 \times 10^{52}$  and  $1.0 \times 10^{53}$  erg/s respectively. The estimated jet power seems to be very huge. However in presented formalism, all quantities are measured in the observers’s frame, thus the radiated power  $P_{rad}$  will be computed directly from the observed SED, unlike to bulk Doppler boosted model where  $P_{rad}$  is measured in the comoving frame.

Moreover the estimated jet power can be reduced by simply using the existence degeneracy between parameters  $n_e$ ,  $\lambda$ , L and R in SED modeling. For example, we can also model the EC dominated case of above mentioned SED of 3C 454.3 for R/L=0.1 with almost same parameters (see figure 7 for R/L = 0.5) and in this case the jet power becomes  $\sim 10^{49}$  erg/s. In same way for PKS 2155-304, we can fit the SED for R/L = 0.05 with similar parameters (see left panel of figure 10 and table 2), the jet power becomes  $10^{49}$  erg/s. For considered SEDs with having jet power  $P_{jet} \sim 10^{49}$  erg/s the inferred R/L would be become  $\lesssim 0.35$ , 0.0001, 0.0002, 0.00015 and 0.0001 for EC, SSC dominated 3C 454.3, OJ 287, S5 0716+714 and PKS 2155-304 SED respectively. In addition the jet power can be decreased by increasing  $n_e$  (which will lower L so R also) as  $P_{jet} \propto n_e R^2$ . In general, the jet power and  $\gamma$ -ray variability time scale combinedly will give a tighter constraint on electron density and the size of the emission region. The respective constraint parameters of all considered cases are summarized in table 4.

**Total averaged electrons energy in the emission region:** The total averaged electrons energy inside the emission region  $W_e$  can be expressed as,

$$W_e = \pi R^2 L n_e m_e c^2 \langle\gamma^R\rangle$$

In above paragraph, we have constrained R/L ratio by fixing  $P_{jet} \sim 10^{49}$  erg/s in addition to the SED modeling (listed in table 4). We compute the total averaged electrons energies for all cases with this sets of parameter.  $W_e = 2.2 \times 10^{53}$ ,  $1.2 \times 10^{54}$ ,  $8.7 \times 10^{53}$ ,  $1.0 \times 10^{54}$  and  $7.1 \times 10^{53}$  erg for EC, SSC dominated 3C 454.3, OJ 287, S5 0716+714 and PKS 2155-304 SED respectively (listed in table 4). Thus, within the jet-activity time scale the maximally pumped energy into the large scales structure of the jet would not be huge,  $\sim 10^{54}$  erg. Hence, the estimated set of parameters is consistent with the observed large scales structure of the jet in terms of the energy budget. Recently, [H. E. S. S. Collaboration et al. \(2020\)](#) have estimated the total energy in electrons  $W_e = 4 \times 10^{53}$  erg for the inner, kiloparsec-scale jet of Centaurus A (note, our estimated  $W_e$  is for the emission region or for a core emission). In addition, the electron cooling due to a synchrotron emission and IC emission will also reduce the total pumped energy into the large scales structure of the jet. The electron cooling also leads to an evolution of the spectral state, mainly, flaring state to the quiescent state. In present calculation, we did not study the evolution of the spectral state self-consistently, however the averaged electron’s Lorentz factor  $\langle\gamma^R\rangle$  decreases from the flaring state to quiescent (see table 1 and 3).

#### 4.5 Estimated $n_e$ of the jet emission region and matter supplied to the jet from the base of the jet

With constraint of optically thin medium for IC, of the  $\gamma$ -ray variability time scale, and of a statistical significant modeled IC spectra, the estimated electron density of the jet emission region is appeared as a large quantity especially for BL Lac objects or only SSC cases. Here, we examine the physicality of large electron density in emission region by estimating the total injected matters into the jet emission region from the inner region of the accretion disk (or from the base of the jet). For this, we compute the total number of electrons inside the emission region of the jet ( $n^{er}$ ) and inside the inner region of the accretion disk ( $n^{dk}$ ). The volume of the inner region of the disk is  $\pi r_{in}^2 h$ , here  $r_{in}$  is the outer radius of the inner region, and  $h$  is the disk scale height. Typically,  $r_{in}$  is the order of  $10 - 30 R_g$  for the base of the jet (e.g. [McKinney 2006](#); [Romero et al. 2017](#)). The ratio of the total number of electrons inside the

Table 4: Constraint source parameters derived from the SED modeling and  $P_{jet} \sim 10^{49}$  erg/s

Parameters	FSRQ (EC)*	FSRQ (SSC)*	LBL*	IBL*	HBL*
L ( $10^{14}$ cm)	5	5	20	20	20
R/L	0.35	1.0e-4	2.0e-4	1.5e-4	2.0e-4
$n_e$ ( $\text{cm}^{-3}$ ) <sup>†</sup>	$10^{12}$	$10^{17}$	$10^{15}$	$10^{15}$	$10^{15}$
$n^{er}/n^{dk}$ <sup>†</sup>	4.0e-7	6.6e-9	4.0e-9	1.6e-9	4.0e-9
$\langle \gamma \rangle^{**}$	321	5289	2507	3828	4764
$\langle \gamma^{ran} \rangle^{**}$	17.5	700	425	575	725
$p$	1.4	2.1	2.1	2.1	2.3
$q$	2.1	4.1	4.1	4.1	5.1
$B_o$ (G)	1.0e-2	3.6e-8	1.6e-6	8.1e-7	3.2e-7
$P_{jet}$ (erg/s)	1.3e49	7.1e49	1.3e49	1.5e49	1.0e49
$W_e$ (erg)	2.2e53	1.2e54	8.7e53	1.0e54	7.1e53

\* FSRQ, LBL, IBL and HBL stand for sources 3C 454.3 (Shah et al. 2017), OJ 287 (Kushwaha et al. 2013), S5 0716+714 (Chandra et al. 2015), and PKS 2155-304 (Gaur et al. 2017) respectively. EC and SSC are for EC and SSC dominated cases for 3C 454.3 respectively.

<sup>†</sup> In some cases  $n_e$  becomes comparable to the inner region of the disk, however the total electrons of the emission region is always 7 orders (i.e.,  $n^{er}/n^{dk} \lesssim 10^{-7}$ ) lesser than the inner disk region. (see text for details)

\*\* in units of  $m_e c^2$

emission region to inside the inner region of the disk is expressed as,

$$\frac{n^{er}}{n^{dk}} = \frac{R^2 L n_e}{r_{in}^2 h n_e^{dk}} \approx \frac{10^3 R^2 L n_e}{r_{in}^3 n_e^{dk}} \quad (6)$$

Above, for approximate expression we use the relation of thin accretion disk ((Shakura & Sunyaev 1973))  $r/h \sim 10^3$  at  $r \sim r_{in}$ , and  $n_e^{dk}$  is the electron density of the disk at  $r_{in}$ . Mostly, the mass of the central black hole in blazars is uncertain. For a rough estimation of the ratio  $\frac{n^{er}}{n^{dk}}$  in case of BL Lac objects, we consider the mass of the black hole  $M_{BH} = 10^8 M_\odot$ , which gives  $n_e^{dk} \sim 10^{18} \text{ cm}^{-3}$  at  $r = 30R_g$  for a mass accretion rate  $\dot{M} = 10^{-2} \dot{M}_{Edd}$  in a thin accretion disk, here  $\dot{M}_{Edd}$  is the Eddington mass accretion rate. From the calculations (see subsection 4.2), we have  $L \sim 2 \times 10^{15} \text{ cm} \approx 100R_g$ ,  $n_e = 10^{15} \text{ cm}^{-3}$ , and  $R/L \lesssim 10^{-2}$  for the BL Lac objects. Thus,  $\frac{n^{er}}{n^{dk}} \approx 10^{-4}$  and  $10^{-6}$  for  $R/L = 10^{-2}$  and  $10^{-3}$  respectively (here,  $r_{in}=L$ ). Crudely, the total number of electrons of emission region of BL Lac ( $M_{BH} = 10^8 M_\odot$ ) is always 6 orders lesser than the total electrons of the inner disk region provided  $R/L \lesssim 10^{-3}$ .

Masses of the central black hole of 3C 454.3, S5 0716+714 and PKS 2155-304 are uncertain and have a wide ranges, which are  $(0.3 - 2) \times 10^9 M_\odot$  (Bonnoli et al. 2011),  $(0.3 - 4) \times 10^9 M_\odot$  (Kaur et al. 2018) and  $(0.3 - 3) \times 10^9 M_\odot$  (Gupta 2014) respectively. The primary black hole mass of OJ 287 (a binary supermassive black hole system) is  $\sim 1.8 \times 10^{10} M_\odot$  (Rodríguez-Ramírez et al. 2020, and references therein). Unlike the rough estimation of the ratio  $n^{er}/n^{dk}$  (in above paragraph), here we estimate this ratio for constraint parameter sets obtained by SED modeling and  $P_{jet}$ . The constraint R/L is 0.35, 0.0001, 0.0002, 0.00015 and 0.0002 and  $n_e$  is  $10^{12}$ ,  $10^{17}$ ,  $10^{15}$ ,  $10^{15}$  and  $10^{15} \text{ cm}^{-3}$  for EC and SSC dominated 3C 454.3, OJ 287, S5 0716+714 and PKS 2155-304 respectively for  $P_{jet} \sim 10^{49}$  erg/s (see section §4.4 or table 4). To compute  $n^{er}/n^{dk}$ , we take an average value of the black hole mass for all sources  $M_{BH} = 10^9 M_\odot$ , and  $r_{in} = 30R_g$ , with this the electron density of the inner region of the disk is  $n_e^{dk} \sim 3 \times 10^{17} \text{ cm}^{-3}$ . The emission region size L is  $\sim 3R_g$  and  $\sim 10R_g$  for considered FSRQ and BL Lac objects respectively. The estimated ratio of electron in emission region to inner region of the disk is  $\frac{n^{er}}{n^{dk}} = \frac{0.12 n_e}{n_e^{dk}}, \frac{2 \times 10^{-8} n_e}{n_e^{dk}}, \frac{1.2 \times 10^{-6} n_e}{n_e^{dk}}, \frac{6.6 \times 10^{-7} n_e}{n_e^{dk}}, \frac{1.2 \times 10^{-6} n_e}{n_e^{dk}}$  for EC and SSC dominated 3C 454.3, OJ 287, S5 0716+714 and PKS 2155-304 respectively (see, table 4). In summary, though the estimated  $n_e$  seems huge but due to a small R/L the total electrons present in emission region size is many orders smaller than the inner region of the disk. That is, the matter of jet emission region has been injected by the inner accretion disk around the central black hole, and thus the estimated electron density of jet's emission region is consistent in terms of the disk-jet connection.

## 5 Summary and Conclusions

Based on the observed jet morphology and a wide range of rarely repeating spectral, temporal, polarization behaviors, we explored blazars broadband SEDs in a locally anisotropic, relativistic flow within a steady conical jet assuming leptonic emission scenario. The highly relativistic velocity along the jet axis dominates to its random perpendicular component. The anisotropically moving electron (along the jet axis) radiates synchrotron emission in forward direction (thus beamed in the forward direction) in presence of helical wiggler plus axial magnetic field where electron follows the helical path without changing its axial velocity component and wiggler field directed random component. Assuming a broken-powerlaw energy distribution of the electrons, we calculate the synchrotron and IC emission from a cylindrical emission region of radius  $R$  and length  $L$ . For the latter, we employ Monte Carlo method. We emphasized that in single scattering limit the photon-photon scattering for pair production does not dominate over IC process. The model SED has a best description of observation when it is generated in single scattering limit. We performed modeling of SEDs of different class of blazars (BLLs: OJ 287 (LBL), S5 0716+714 (IBL), PKS 2155-304 (HBL); FSRQ: 3C 454.3)) in their different flux states and also explore the effects of geometry on the parameters and observed emission. The observed short  $\gamma$ -ray variability has been explained in terms of electron density, since the free parameters  $n_e$ ,  $\lambda$ ,  $L$  are degenerate in the IC process. For example, ten hours variability of flaring state of 3C 454.3 is explained with  $n_e \gtrsim 10^{12} \text{ cm}^{-3}$  in EC dominated case (also we have estimated the seed photon density for EC, which is  $\sim (15-135) n_e$ ). Two days variability of OJ 287 is described with high  $n_e \gtrsim 10^{15} \text{ cm}^{-3}$  for  $\langle \gamma^{ran} \rangle = \gamma_{min}/2$ . However, this apparently large  $n_e$  is due to the requirement that SSC reproduces the observed spectra in single scattering limit. Moreover, we have shown that the total electrons present in emission region size is always 7 orders smaller than the inner region of the disk, i.e., the matter of jet emission region has been injected by the inner accretion disk around the central black hole.

We also explored the effect of dimension on the observed broadband spectrum and found that high energetic emission of LSP blazar can be explained through SSC only by decreasing the radius to length ratio ( $R/L$ ) of cylindrical emission region ( $R/L < 0.001$ ). However, this also results in a significant fraction of unscattered photons leaving from side rather than the front face of the cylindrical emission region. For example, the flaring phase of 3C 454.3 has almost an order of magnitude more emission at  $\gamma$ -ray compared to the synchrotron part and we can model this SED considering SSC only. The estimated  $R/L$  is  $\lesssim 0.0001$  and the associated 10 hours variability is explained with  $n_e \gtrsim 10^{17} \text{ cm}^{-3}$ . We find that for all considered SEDs, the jet is a matter dominated. The estimated jet power is consistent with observed radiative power and constrain tightly the emission region size and electron density along with  $\gamma$ -ray variability. Conclusively, in a steady conical jet assuming leptonic emission scenario and anisotropic flow in helical periodic magnetic field plus axial field, one can modeled the blazar SED successfully; the radiation is beamed, but not by bulk Doppler boosting, and is unaffected from the pair-production.

## Acknowledgements

NK is supported by University Grant Commission (UGC), New Delhi, India through Dr. D.S. Kothari Post-Doctoral Fellowship (201718-PH/17-18/0013). NK thanks Banibrata Mukhopadhyay of IISc for discussion. NK likes to acknowledge his IUCAA visit (April 2019) and thanks Dipankar Bhattacharya and Ranjeev Misra for critical comments and suggestions over the manuscript.

## Data availability

The data is taken from following published work –

[Figure: 5] [Kushwaha et al. \(2018a\)](#)

[Figures: 6a; 7; 8; 9; 11 ] [Shah et al. \(2017\)](#)

[Figures: 6b 10a] [Kushwaha et al. \(2013\)](#)

[Figure: 10b] [Chandra et al. \(2015\)](#)

[Figure: 10c] [Gaur et al. \(2017\)](#)

## References

- Agudo, I., Marscher, A. P., Jorstad, S. G., et al. 2013, arXiv e-prints, arXiv:1303.2039
- Aharonian, F. A., Khangulyan, D., & Costamante, L. 2008, MNRAS, 387, 1206
- Algaba, J. C., Lee, S. S., Rani, B., et al. 2019, arXiv e-prints, arXiv:1905.06621
- Armstrong, C. K., Litvinenko, Y. E., & Craig, I. J. D. 2012, ApJ, 757, 165
- Balal, N., Bandurkin, I. V., Bratman, V. L., Magory, E., & Savilov, A. V. 2015, Applied Physics Letters, 107, 163505
- Blandford, R. D. & Payne, D. G. 1981, MNRAS, 194, 1033
- Bonnoli, G., Ghisellini, G., Foschini, L., Tavecchio, F., & Ghirlanda, G. 2011, MNRAS, 410, 368
- Böttcher, M., Reimer, A., Sweeney, K., & Prakash, A. 2013, ApJ, 768, 54
- Chandra, S., Zhang, H., Kushwaha, P., et al. 2015, ApJ, 809, 130
- Dermer, C. D. & Giebels, B. 2016, Comptes Rendus Physique, 17, 594
- Dondi, L. & Ghisellini, G. 1995, MNRAS, 273, 583
- Fossati, G., Maraschi, L., Celotti, A., Comastri, A., & Ghisellini, G. 1998, MNRAS, 299, 433
- Freund, H. P. & Drobot, A. T. 1982, Physics of Fluids, 25, 736
- Friedland, L. 1980, Physics of Fluids, 23, 2376
- Gabuzda, D. 2017, Galaxies, 5, 11
- Gaur, H., Chen, L., Misra, R., et al. 2017, ApJ, 850, 209
- Ghisellini, G. & Tavecchio, F. 2009, MNRAS, 397, 985
- Ghisellini, G., Tavecchio, F., Maraschi, L., Celotti, A., & Sbarrato, T. 2014, Nature, 515, 376
- Ginzburg, N. S. & Peskov, N. Y. 2013, Physical Review Accelerators and Beams, 16, 090701
- Goyal, A., Stawarz, L., Zola, S., et al. 2018, ApJ, 863, 175
- Gupta, A. C. 2014, Journal of Astrophysics and Astronomy, 35, 307
- H. E. S. S. Collaboration, Abdalla, H., Adam, R., et al. 2020, Nature, 582, 356
- Kaur, N., Baliyan, K. S., Chandra, S., Sameer, & Ganesh, S. 2018, AJ, 156, 36
- Kumar, N. 2017, arXiv e-prints, arXiv:1708.04427
- Kumar, N. 2018, Journal of Astrophysics and Astronomy, 39, 13
- Kumar, N. & Misra, R. 2016, MNRAS, 461, 4146
- Kushwaha, P., Gupta, A. C., Wiita, P. J., et al. 2018a, MNRAS, 473, 1145
- Kushwaha, P., Gupta, A. C., Wiita, P. J., et al. 2018b, MNRAS, 479, 1672
- Kushwaha, P., Sahayanathan, S., Lekshmi, R., et al. 2014, MNRAS, 442, 131
- Kushwaha, P., Sahayanathan, S., & Singh, K. P. 2013, MNRAS, 433, 2380
- Lyutikov, M., Pariev, V. I., & Gabuzda, D. C. 2005, MNRAS, 360, 869
- Maraschi, L., Ghisellini, G., & Celotti, A. 1992, ApJ, 397, L5
- Marscher, A. P. 2006, in American Institute of Physics Conference Series, Vol. 856, Relativistic Jets: The Common Physics of AGN, Microquasars, and Gamma-Ray Bursts, ed. P. A. Hughes & J. N. Bregman, 1–22
- Marscher, A. P. 2014, ApJ, 780, 87
- McKinney, J. C. 2006, MNRAS, 368, 1561
- Pellegrini, C., Marinelli, A., & Reiche, S. 2016, Reviews of Modern Physics, 88, 015006
- Pozdnyakov, L. A., Sobol, I. M., & Syunyaev, R. A. 1983, Astrophysics and Space Physics Reviews, 2, 189
- Rodríguez-Ramírez, J. C., Kushwaha, P., de Gouveia Dal Pino, E. M., & Santos-Lima, R. 2020, MNRAS, 498, 5424
- Romero, G. E., Boettcher, M., Markoff, S., & Tavecchio, F. 2017, Space Sci. Rev., 207, 5
- Shah, Z., Sahayanathan, S., Mankuzhiyil, N., et al. 2017, MNRAS, 470, 3283
- Shakura, N. I. & Sunyaev, R. A. 1973, A&A, 500, 33
- Sikora, M., Begelman, M. C., Madejski, G. M., & Lasota, J.-P. 2005, ApJ, 625, 72
- Titarchuk, L., Mastichiadis, A., & Kylafis, N. D. 1997, ApJ, 487, 834
- Yang, Y.-P. & Zhang, B. 2018, ApJ, 864, L16
- Zdziarski, A. A. 2014, MNRAS, 445, 1321

## A Synchrotron emission by anisotropically moving electron in wiggler plus axial magnetic field

We are revisiting the single relativistic electron trajectory in the periodic helical (wiggler) magnetic field and axial field (studied by [Friedland 1980](#); [Freund & Drobot 1982](#)) and discussed the synchrotron emission by electron with application to our scenario. The combined magnetic field, axial (of amplitude  $B_o$ ) plus wiggler (of amplitude  $B_w$ ) is defined as

$$\mathbf{B} = B_o \mathbf{k} + B_w (\mathbf{i} \cos(k_w z) + \mathbf{j} \sin(k_w z))$$

here,  $2\pi/k_w$  is the wiggler period;  $(\mathbf{i}, \mathbf{j}, \mathbf{k})$  are the cartesian axis where  $\mathbf{k}$  is along the jet-axis. The velocity components of electron are  $v_1, v_2, v_3$  where  $v_3$  is along the  $\mathbf{k}$ -axis and  $v_1$  is along the wiggler field direction while  $v_2$  is perpendicular to  $v_1$  in  $(\mathbf{i}, \mathbf{j})$ -plane. The equation of motion is written as,

$$\dot{v}_1 = v_2(k_w v_3 - \Omega_o); \quad \dot{v}_2 = -\Omega_w v_3 - v_1(k_w v_3 - \Omega_o); \quad \dot{v}_3 = \Omega_w v_2$$

where  $\Omega_o = \frac{eB_o}{\gamma m_e c}$ ,  $\Omega_w = \frac{eB_w}{\gamma m_e c}$ ,  $\gamma = \left(1 - \frac{v^2}{c^2}\right)^{-1/2}$ ,  $v^2 = v_1^2 + v_2^2 + v_3^2$ , and  $\dot{v}_i$  is the time derivative of velocity  $v_i$ . The equation of motion obeys two constant of the motion, i) the total energy is conserved, i.e.,  $v^2 = \text{constant}$ ; ii)  $u = v_1 - k_w \frac{(v_3 - \frac{\Omega_o}{k_w})^2}{(2\Omega_o)} = \text{constant}$ . By using the constant of motion the equation of motion will reduce to

$$\dot{v}_3^2 = \phi(v_3, v, u)$$

where  $\phi(v_3, v, u)$  is a quartic equation for variable  $v_3$ . The real roots of  $\phi$  correspond to the solution  $v_3 = \text{constant}$ ,  $v_1 = \frac{-\Omega_w v_3}{k_w v_3 - \Omega_o}$ , and  $v_2 = 0$  (termed as constant axial velocity solution). The electron follows the wiggler trajectory and radiates synchrotron emission in forward direction.

In above description a non-relativistic energy equation has been considered, as a result in constant axial velocity solution the both velocity components  $v_1$  and  $v_3$  cannot be relativistic together, i.e., for relativistic  $v_3$  the other velocity component  $v_1$  would be non-relativistic and vice-versa. But when one considers a relativistic energy equation (i.e.,  $v^2 = v_1^2 + v_3^2 + v_2^2 \frac{1}{\gamma_1 \gamma_3}$  where  $\gamma_1, \gamma_3$  are the Lorentz factor for velocity  $v_1$  and  $v_3$  respectively) then both  $v_3$  and  $v_1$  can be relativistic, which is our considered case. Thus, the both velocity components of electron can be relativistic in this field configuration (e.g., [Pellegrini et al. 2016](#)).